Ore Geology Reviews 139 (2021) 104516

Contents lists available at ScienceDirect

Ore Geology Reviews

journal homepage: www.elsevier.com/locate/oregeorev

The genesis and mineralization process of Xiaobaliang VHMS Cu-Au deposit, Central Asian Orogenic Belt: Constraints from the pyrite geochemistry and zircon geochronology

Fanghua Zhang [a], Wenbo Li [a,*], Chuansheng Hu [a], Tianyao Fu [a], Xueyuan Qiao [a], Lejun Zhang [b]

[a] Key Laboratory of Orogenic Belt and Crustal Evolution, School of Earth and Space Sciences, Peking University, Beijing 100871, China
[b] ARC Centre of Excellence in Ore Deposits (CODES), University of Tasmania, Private Bag 79, Hobart 7001, Australia

ARTICLE INFO

Keywords:
LA-ICP MS
Trace elements
Xiaobaliang deposit
Xing'an-Mongolia Orogenic Belt (XMOB)

ABSTRACT

The Xiaobaliang Cu-Au deposit is located in the Hegenshan ophiolite complex belt of the western Xing'an–Mongolia Orogenic Belt (XMOB). Strata-bound sulfide ores are discovered within the Carboniferous volcanic tuff, with the oxidized Au-Cu ores at the top and Cu (-Au) sulfide ores at the bottom. Zircon U-Pb dating on volcanic tuff has yielded a concordia age of 326 ± 3 Ma (n = 21, MSWD = 5.6). Four types of pyrite have been identified, including lamellar pyrite (Py1) in the wall rocks, framboidal pyrite (Py2) in the Zn-rich massive ores, colloform pyrite (Py3) in the massive Cu ores, and euhedral pyrite (Py4) in the fractured Cu ores. Chalcopyrite comprises two types: early massive chalcopyrite aggregates (Cp1) and late chalcopyrite veinlets (Cp2). Here we present the in situ trace elements and sulfur isotopes analyses of different sulfide generations. Elements like Se (44.1 ppm), Co (227 ppm) and Cu (3211 ppm) are enriched in pyrites from Cu ores (Py3&Py4), whereas the pyrites from altered rocks (Py1) take high Mn (5027 ppm), Ti (134 ppm), V (13.0 ppm), Ni (41.9 ppm) and Au (5.07 ppm) concentrations. Similar elemental patterns are observed in chalcopyrite analyses where Co (312 ppm), Se (566 ppm) and Te (31.5 ppm) are enriched in massive Cu ores (Cp1), but Mn (147 ppm), V (174 ppm) and Ti (42.2 ppm) contents are mainly concentrated in chalcopyrite veinlets (Cp2). In situ S isotope analyses exhibit a large variation in Py1 (−30.70 to −1.50‰) and Cp2 (−7.81 ~ −4.50‰) but are constant in Py2, Py3, Py4 and Cp1 (0.44 to 3.15 ‰). The high Co/Ni ratios and relatively lower $\delta^{34}S$ values in Py1 suggest a diagenetic environment where the lower-temperature and extremely reduced conditions facilitate the enrichment of Mn, V and Au. The progressive enrichment of Sn, Te, Bi, Se and Cu in hydrothermal Py3 and Py4 then points out the rising of temperature in the weakly reduced environment. The negative sulfur isotopes in altered rocks (Py1) and fractured ores (Cp2) point out the contribution of the volcanic-sedimentary sequence. These compositional features, combined with sulfur isotopes, have demonstrated that Cu was mainly derived from magmatic-hydrothermal fluids whereas Au was released from Au-rich sediments on the seafloor. The Xiaobaliang Cu-Au deposit belongs to a Cyprus-type VHMS deposit formed in the Carboniferous extensional setting.

1. Introduction

Since the discovery of active hydrothermal vent system in modern seafloor, the ancient submarine hydrothermal system has attracted much attention for its role in both life origin and ore formation (Franklin et al., 2005; Martin et al., 2008; Piercey, 2011; Hannington, 2013; Tornos et al., 2015; Zhang et al., 2020). The stratiform or strata-bound accumulation of metals and sulfides in ancient seafloor has contributed to the formation of volcanic-hosted massive sulfide (VHMS) deposits, where submarine volcanic rocks act as an important constituent (Franklin et al., 2005; Galley et al., 2007). Volcanic-hosted massive sulfide deposits occur throughout geological time and tectonic domain. They are major sources of Cu and Zn, as well as significant quantities of Pb, Au, Ag (Galley et al., 2007; Maslennikov et al., 2009; Maslennikov et al., 2017). The Central Asian Orogenic Belt (CAOB) has witnessed the accretion of ocean crust, island arc and microcontinent to the active margins of ancient Siberia, Baltica, Tarim and North China Cratons since 1.0 Ga (Sengör et al., 1993; Xiao et al., 2003; Windley et al., 2007; Xu et al., 2014). Many large VHMS deposits were therefore preserved in this accretionary orogen from the northwest Uralian terrane (Mason et al.,

* Corresponding author.
E-mail address: liwenbo@pku.edu.cn (W. Li).

https://doi.org/10.1016/j.oregeorev.2021.104516
Received 17 June 2021; Received in revised form 17 August 2021; Accepted 19 August 2021
Available online 9 October 2021

2005; Maslennikov et al., 2013) to the central west Altaides terrane (Wan et al., 2010; Zheng et al., 2013, 2016; Yu and Zheng, 2019; Yu et al., 2020).

In the southeastern segment of the CAOB, however, no VHMS deposit has been previously reported except for Bieluwutu (Li et al., 2021). Recent fieldwork has discovered the Xiaobaliang Cu-Au deposit in the Hegenshan ophiolite complex belt of the southeastern CAOB. The Hegenshan ophiolite complex was located at the suture between the Siberian Craton and North China Craton (NCC) (Nozaka and Liu, 2002; Jian et al., 2012). There are different views on the type and origin of Xiaobaliang Cu-Au deposit. Based on the geological, lithogeochemical and isotopic features, Chen et al. (1995) firstly proposed that it was a VHMS deposit formed in the mid-ocean ridge tectonic setting at 243 ± 15 Ma (Rb-Sr dating). Lateral geochemical studies on quartz-keratophyre and cherts suggested an intraplate rifting environment and related hydrothermal sedimentation process (Wang, 2008; Sun et al., 2009). Further research on the surrounding tuffs then pointed out a Late Carboniferous VMS-type Cu-Au mineralization event (Gao, 2019). However, Nie et al. (2007) and Gong (2012) argued that it was a magmatic-hydrothermal deposit for its spatial relationship with dolerite and isotopes similar to the magmatic source. The geochemistry similarities between the host tuffs and other basaltic-andesitic rocks within the Hegenshan ophiolite belt also indicated the connection between mineralization and magmatism (Gong, 2012).

Many different ideas were also proposed on the emplacement age, origin and tectonic setting of Hegenshan ophiolite (Nozaka and Liu, 2002; Miao et al., 2008; Zhou et al., 2015; Jiang and Zhu, 2019), in either Paleozoic back-arc setting or Mesozoic mid-ocean ridge environment. The variety of metal assemblages in VHMS deposits depends on surrounding volcanics and tectonic settings (Franklin et al., 2005; Gibson, 2005; Piercey, 2011). Juvenile, mafic-dominated VHMS environments in the middle ridge, island arc, and continent rift settings typically show an affinity to Cu, Zn, Co and Platinum Group Elements (Oudin and Constantinou, 1984; Maslennikov et al., 2009; Piercey, 2011). The proportion of Zn and Pb would otherwise increase in the evolved continental arc to back-arc environments where felsic volcanics are widely distributed (Piercey, 2011). Furthermore, the gold-rich VHMS deposits are commonly associated with calc-alkaline intermediate to felsic volcanic rocks in the early rifting environment (Mercier-Langevin et al., 2011). Thus, identifying the metal assemblage at the Xiaobaliang deposit would also help to ascertain its tectonic setting, as either continental rifting or bac-arc environment.

As for volcanic-hosted massive sulfide deposits, its metal zoning and ore deposition process are also sensitive to the physicochemical condition of the hydrothermal system. The compositional variations of the sulfide ores could provide robust evidence reflecting the conditions of ore formation. Laser ablation (multi-collector) inductively coupled plasma mass spectrometry (LA-(MC)-ICP-MS) is a useful tool for analyzing trace element and sulfur isotope compositions of sulfides (Butler and Nesbitt, 1999; Cook et al., 2009; Large et al., 2009;

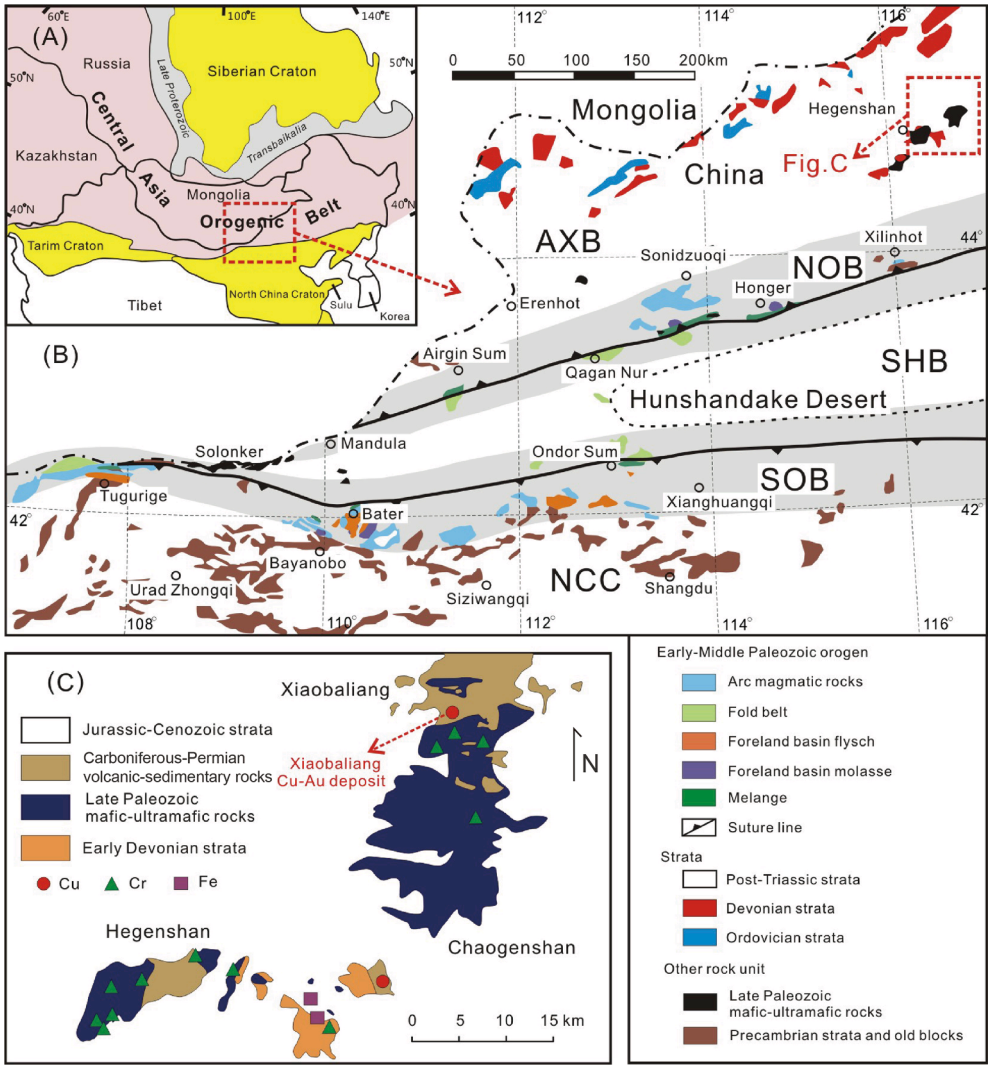

Fig. 1. (A) Tectonic framework of the Central Asian Orogenic Belt. Major cratons are in yellow. (B) Simplified geological map of the western Xing'an–Mongolia Orogenic Belt (XMOB), showing the location of the study area (modified after Xu et al., 2013). NCC, North China Craton; SOB, Southern Orogenic Belt; SHB, Songliao-Hunshandak Block; NOB, Northern Orogenic Belt; AXB, Airgin Sum-Xilinhot Block. (C) Simplified geological map of the Hegenshan ophiolite complex area, showing the location of the Xiaobaliang Cu-Au deposit and the adjacent chromium, copper and iron deposits and ore spots. (For interpretation of the references to colour in this figure legend, the reader is referred to the web version of this article.)

Maslennikov et al., 2009; Dehnavi et al., 2018). These in situ analyses would help for evaluating the relationship between volcanism and metal deposition.

This paper reported the age of the host volcanic rock, geological features of the deposit, geochemical and isotopic compositions of sulfides from the deposit. The aim is to clarify the origin of the ore-forming metals and to clarify the mechanisms of ore formation. It is not only aimed at understanding the genesis of the deposit, but also has important implications for understanding the tectonic setting and aiding VHMS deposits exploration in the southeastern CAOB.

2. Regional geology

The Central Asian Orogenic Belt (CAOB) is the largest Phanerozoic accretionary orogenic belt in the world, characterized by multiple phases of island-arc growth, back-arc rifting, and terrane accretion (Fig. 1A; Sengör et al., 1993; Badarch et al., 2002; Jahn, 2004; Windley et al., 2007; Kröner et al., 2014). The Xing'an–Mongolia Orogenic Belt (XMOB) is the southeastern segment of the CAOB. It is located between the Siberian Craton to the north and the North China Craton (NCC) to the south (Fig. 1A). The XMOB formed via the amalgamation of several microcontinental blocks, island arcs, and remnants of oceanic crust. The timing of the final collision has long been debated, varying from late Devonian to early Mesozoic (Tang, 1990; Shao, 1991; Chen et al., 2000; Xiao et al., 2003; Xu et al., 2013; Domeier and Torsvik, 2014). Xu et al. (2013) subdivided the western XMOB into four tectonic units (Fig. 1B). namely Airgin Sum-Xilinhot Block (AXB), Northern Orogenic Belt (NOB), Songliao-Hunshandak Block (SHB) and the Southern Orogenic Belt (SOB) from north to south. The XMOB had gone through strong post-collisional extension and eventually formed a stable continent in the early Triassic (Xu et al., 2013; Shao et al., 2014; Xu et al., 2014). Manly medium to large size deposits are distributed in the west part of XMOB and related to the evolution of the Paleo-Asian Ocean (500–210 Ma), including the magmatic Cu-Ni and Cr deposits (e.g., Solunshan, Ebutu; Jiang et al., 2018), porphyry Cu-Mo, Mo, Au deposits (e.g., Haolibao, Bilihe, Zhunsujihua; Qing et al., 2011; Liu et al., 2012; Zeng et al., 2013), orogenic gold deposits (e.g., Bayinbaolidao, Saiyinwusu; Jiang et al., 2018) and skarn Pb-Zn deposits (e.g., Baiyinnuoer; Zeng et al., 2009).

The Airgin Sun-Xilinhot Block mainly consists of early Neoproterozoic metamorphic basements (>950 Ma), early Paleozoic arc-related magmatic rocks (490–430 Ma), Devonian molasse formation and Carboniferous volcanic-sedimentary rocks (Xu et al., 2014). The southern margin of the AXB has many outcrops of mafic–ultramafic rocks, including the Hegenshan (ca. 60 km^2) in the west and Chaogenshan-Xiaobaliang (ca. 200 km^2) in the east (Fig. 1C; Jian et al., 2012). The mafic–ultramafic rocks were ascribed collectively to a single lithological unit, named the Hegenshan ophiolite (Robinson et al., 1999). The bulk of these ophiolites were considered to have formed in the Late Carboniferous to Early Permian, based on zircon U-Pb ages of 354–295 Ma (Miao et al., 2008; Jian et al., 2012). The ophiolites are unconformably overlain by the Late Carboniferous to Early Permian volcanic-sedimentary sequences that host the Xiaobaliang Cu-Au deposit (Fig. 1C). All the aforementioned strata are overlain by widely distributed post-Triassic cover sequences (Fig. 1C). Apart from the mafic–ultramafic rocks, other intrusions in this region are uncommon. Numerous chromium, copper and iron deposits and ore spots have been discovered within the mafic–ultramafic rocks and volcanic-sedimentary strata, which are an ideal target area for mineral exploration in Inner Mongolia (Nie et al., 2007).

3. Deposit geology

The Xiaobaliang Cu-Au deposit is situated between the Xiaobaliang and Chaogenshan ophiolitic complexes (Fig. 1C). The only stratigraphic unit in the district is the Carboniferous-Permian Egenaobao Formation, a volcano-sedimentary sequence comprising trachybasalt, trachyandesite, tuff, tuffaceous sandstone and siltstone (Fig. 2). The volcano-sedimentary units were previously interpreted to have formed on the seafloor during volcanism and sedimentation in the Early Permian (Chen et al., 1995). In addition to the tuffs, volcanic rocks are widely distributed in the whole district, including spilite, quartz-keratophyre, volcanic breccia, and basalt, associated with minor gabbro (Fig. 2). Nie et al. (2007) argued that the spilite was actually dolerite dykes, derived from a Na-rich alkaline mafic magma. To the north of Xiaobaliang district, there are also some mafic and felsic intrusions formed between 359 and 333 Ma (Jian et al., 2012; Huang et al., 2021). Minor mafic dikes of the Cretaceous era were outcropped in the Hegenshan area, about 5 km south of Xiaobaliang district (Huang et al., 2021). There is no alteration or mineralization developed within quartz-keratophyre, gabbro and other mafic dikes. The orebodies of Xiaobaliang are hosted in basalt and andesitic tuff.

3.1. Orebody and alteration

The orebodies are lenticular or quasi stratiform, and are discontinuously distributed in the wall rocks from the west to the east of the ore district (Fig. 2), and controlled by the NEE trending faults. In cross-section the orebodies are stratiform, extending ca. 120–200 m down dip in stratigraphy that dips 60°–75° to the south (Fig. 3). A total of 34 orebodies have been identified so far, and contacts between the orebodies and wall rocks are gradational. The wall rocks are mostly altered to chlorite, sericite, quartz and carbonate.

Two types of ores are recognized at Xiaobaliang: primary Cu (-Au) sulfide ores and oxidized Au-Cu ores. The primary Cu ores account for>80% of total reserves, with an average Cu grade of 0.7–2.0 wt% (Chen et al., 1995, Fig. 4). Locally, several Zn-rich zones have been found in Cu ores, and there is an apparent metal zoning pattern of chalcopyrite-rich ore gradually changing to sphalerite-rich ores (Fig. 5B, Fig. 4). The primary Au-rich zones were discovered in altered andesitic tuff where pyrite and chlorite are abundant (Fig. 4C). The gold content in sulfide ores is generally below 1 g/t, thus no free gold was observed under the microscope. These elemental variations have been identified in primary halos diagrams (Fig. 4). Metals like Cu and Zn were mainly concentrated in the footwall trachybasalt and make up the Cu (-Zn) sulfide ores. Nevertheless, gold was mainly enriched in the andesitic tuff from the hanging wall and exhibits less connection with the underlying trachybasalt (Zhang et al., 1991; Gao, 2019). The oxidized Au ores, with an average gold grade of 4.6 g/t, are concentrated in the upper orebodies (Fig. 4C). The dominant sulfides in the primary Cu ores are chalcopyrite, pyrite, bornite, marcasite, sphalerite and minor galena. Major gangue minerals are chlorite, quartz, calcite, feldspar and pyroxene. Minerals in the oxidized ores include limonite, hematite, malachite, azurite, cuprite, jarosite and native gold.

Hydrothermal alteration in Xiaobaliang is extensively developed in the orebodies and wall rocks. Some tuff fragments have been cemented by chlorite-bearing sulfide veins (Fig. 5A). Typical hydrothermal minerals are chlorite, muscovite, quartz, carbonate and clay minerals. Chlorite alteration was discovered in the orebodies and surrounding dolerite or andesite tuffs, where pyroxene and hornblende were replaced by chlorite. Muscovite, or sericite named in fieldwork, has developed along with chlorite alteration and replaced plagioclase. These two alteration zones are 5 – 10 m wide and commonly overlapped by silicate alteration. Hydrothermal quartz occurs on the edge of the chlorite and sericite alteration zone and fills the fractures of breccia (Fig. 5C). Some quartz veins even separately occur around the edge of andesitic tuff (Fig. 5E). The tuffs and their surrounding quartz veins were then cemented by lateral pyroclasts. Carbonate minerals like calcite occur on the hanging wall or distal area. The orebodies near the ground surface were oxidized and the supergene zone is about 30 to 60 m thick (Fig. 5A). Sulfides were oxidized to hematite, limonite, malachite, jarosite while silicate minerals were converted to kaolinite.

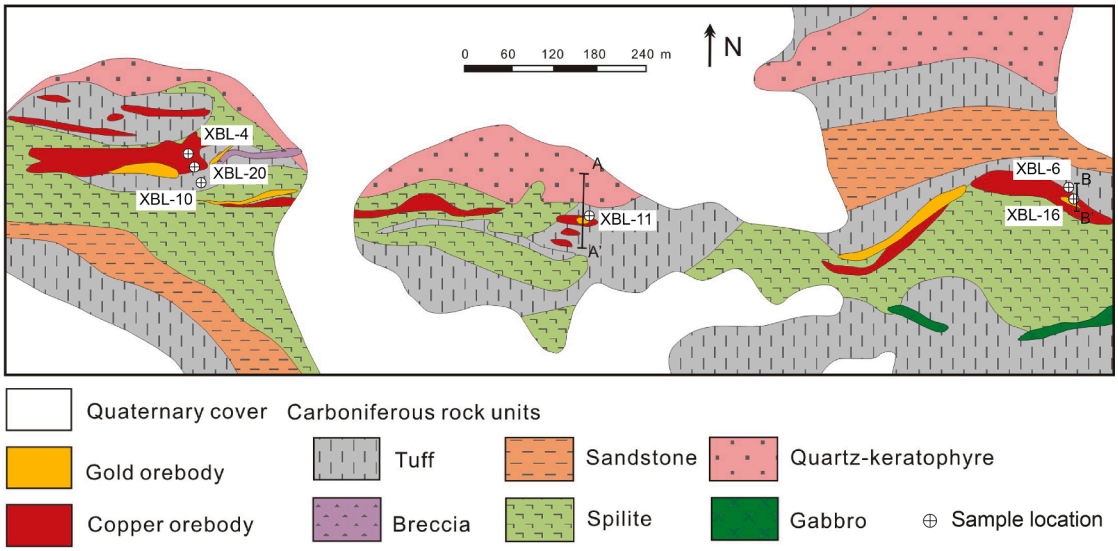

Fig. 2. Geological map of the Xiaobaliang ore district, showing the location of the geologic cross-section (modified after Chen et al., 1995).

3.2. Types of pyrite and chalcopyrite

Pyrite and chalcopyrite are the dominant sulfide minerals at Xiaobaliang. Here we collected the sulfides from altered andesitic tuff (XBL-11/16, Fig. 5E), Zn-rich Cu ores (XBL-6, Fig. 5D), massive Cu ores (XBL-4, Fig. 5D) and fractured Cu Ores (XBL-20, Fig. 5C). The altered andesitic tuff is composed of tuff fragments. Hydrothermal quartz veins are typically formed at the edge of fragments and cemented by the chlorite-bearing sulfide veins. Field observations have discovered the transition zone in Cu-Au sulfide ores, from the massive Cu ore in the center, through the Zn-rich Cu ores in the rim, to the altered andesitic tuff in the outer space. There are also some fractured Cu ores at the bottom of the orebodies, where the chlorite alteration zone was cut by quartz-sulfide veins.

Based on morphology, grain size, paragenesis and distribution, four types of pyrite have been identified in this study, including lamellar (Py1), framboidal (Py2), colloform (Py3) and euhedral pyrite (Py4). The lamellar pyrite (Py1) consists of tabular shapes with a thickness of 50–200 μm. This type of pyrite is preferentially hosted in tuffaceous sandstone and andesitic tuff (Fig. 6A), either as veins within tuff fragments or disseminated in the cement. Meanwhile, the altered andesitic tuff exhibits a relatively higher Au anomaly where the sulfide is abundant (Zhang et al., 1991; Fig. 4C). The framboidal (Py2) grains mainly occur in the Zn-bearing Cu sulfide ores and tuffaceous siltstone. They display typical framboid textures of pyrite microcrystals in spheres from 10 to 30 μm in diameter (Fig. 6B). They are commonly surrounded by Py3 and marcasite (Fig. 6C). Py3 has colloform textures with bands 0.1–0.4 mm in thickness. Py3 is found in both the Cu-rich and Zn-rich ores. Py3 commonly has a marcasite core that is 100–500 μm in diameter (Fig. 6D). Most of the Py3 and marcasite have been replaced by chalcopyrite (Fig. 6E). Py4, presents as coarser-grained euhedral to subhedral clusters with grain sizes of 100–300 μm, is widely distributed in the main massive and fractured Cu ores (Fig. 6F).

Chalcopyrite is distributed widely in the Cu ores and wall rocks and can be divided into two types: massive chalcopyrite aggregates (Cp1) and chalcopyrite veinlets (Cp2). Cp1 is a homogeneous, featureless type of chalcopyrite, commonly intergrown with Py4. This is the dominant type of chalcopyrite in the massive Cu ores. Cp1 fills fractures in both Py3 and Py4, with abundant pyrite inclusions (Fig. 6E-G). This type of chalcopyrite commonly replaces Py3 and sphalerite, forming a distinct chalcopyrite disease texture in sphalerite (Fig. 6H). In contrast, Cp2 mainly occurs as irregular veinlets that cut sphalerite (Fig. 6I).

Based on the mineral textures and paragenetic relationships (Fig. 7), Py1, Py2 and Py3 are considered to have formed in the early stage of mineralization. The massive chalcopyrite (Cp1) commonly formed together with Py4 or occasionally coexisted with Py3, whereas veined Cp2 precipitated later.

4. Analytical methods

4.1. Zircon U-Pb analysis

The least altered tuffs from Xiaobaliang Cu-Au deposit are mainly basalt and andesite. Here we chose andesitic tuff (XB-10) that hosted the orebody for geochronology research. Zircon grains were separated from crushed rocks using conventional heavy liquid and magnetic methods. These grains were further observed under an optical microscope and cathodoluminescence (CL) after the casting of the epoxy mount. All together twenty-one zircon grains with the uniform structure were selected for analysis. The LA-ICP-MS zircon U-Pb and trace elements analyses were conducted at the Key Laboratory of Orogenic Belts and Crustal Evolution, School of Earth and Space Sciences, Peking University. A GeolasPro laser ablation system with an optical system and an ArF excimer laser system (~193 nm) was used for laser ablation. An Agilent 7500CE ICP-MS instrument was used for ion-signal intensity acquisition. The laser spot was set to 32 μm with the frequency of 5 Hz and energy density of 10 J/cm^2. Zircon Plešovice was analyzed for isotopes and age calibration while 91,500 was tested as a secondary standard. Trace elements were calibrated using Si as internal standard and NIST 610 as external standard. Off-line selection, signal integration and isotope/element calibration were processed using the program Glitter (Van-Achterbergh et al., 2001). Common lead correction followed the method of Andersen (2002). Geochronology calculations and diagrams were made using Isoplot/Ex_ver3 (Ludwig, 2003).

4.2. Sulfide trace elements analysis

As the oxidized Au ores at the Xiaobaliang deposit have already been mined out, the samples collected in this study were all from the primary Cu ores and the sulfide-bearing wall rocks. Quantitative analysis of sulfides for a wide range of major and trace elements (Fe, Cu, Zn, Co, Ni, Au, Ag, Bi, Pb, Tl, Cd, As, Te, Se, Mo, V, Ti, and Mn) were determined using laser-ablation inductively coupled plasma mass spectrometry (LA-ICP MS) at CODES, University of Tasmania. Analytical instruments employed in this study were a New Wave UP-213 nm Laser Ablation System coupled with an Agilent 7700 s Quadrupole ICP MS. Analyses

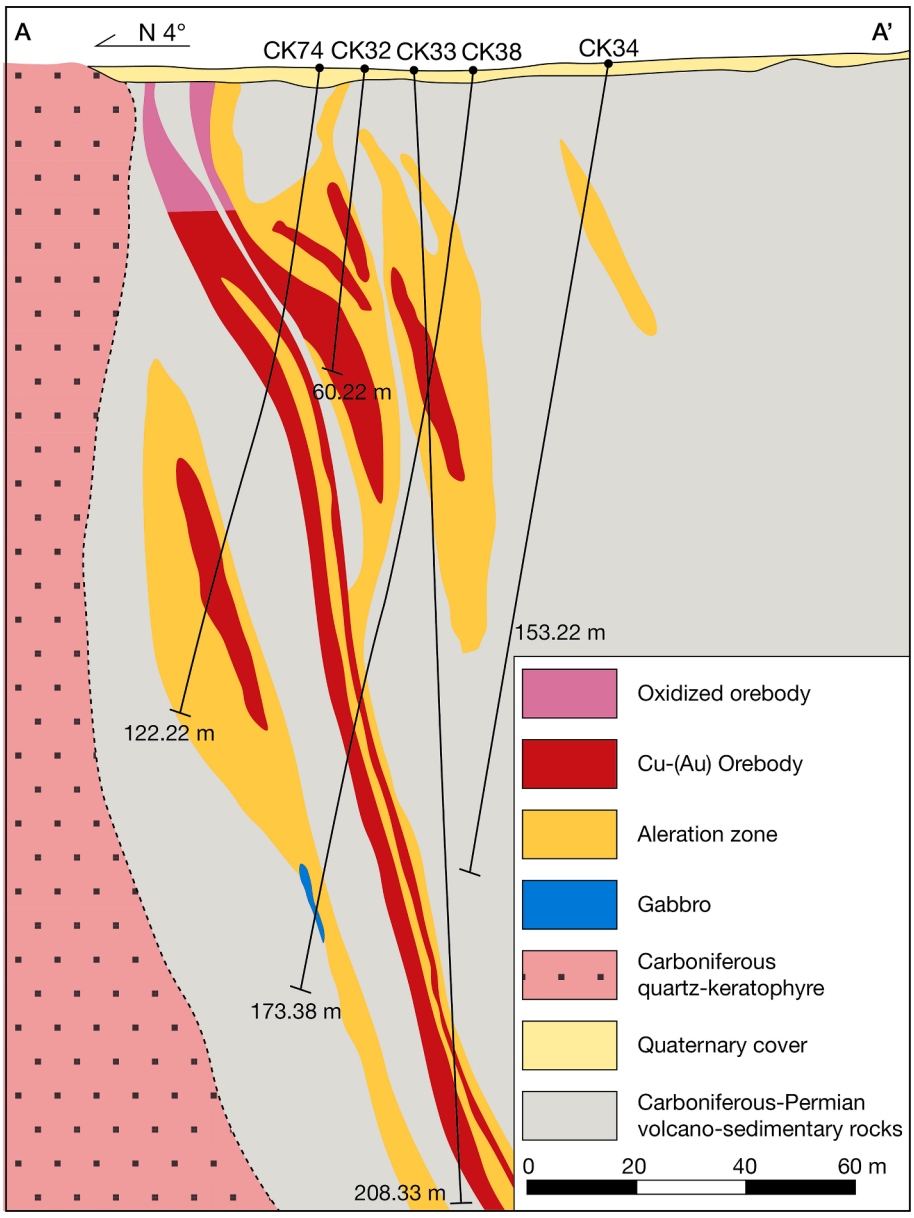

Fig. 3. Geological cross-section (A-A') of the Xiaobaliang Cu-Au deposit with the drill holes (modified after Nie et al., 2007).

were performed in an atmosphere of pure He.

The quantitative analyses for this study were performed in spot mode using a laser beam of 40 μm, a repetition rate of 5 Hz and laser energy of 4–5 J/cm^2. Each analysis time was 90 s, comprising a 30 s measurement of background with laser-off and a 60 s analysis with laser on. Acquisition time was set to 0.02 s, with a total sweep time of ~ 0.6 s. Data reduction was performed based on standard methods by Longerich et al. (1996). All analyses were quantified against STDGL2b2 standard, which comprises powdered sulfides doped with certified element solutions and fused to a lithium borate glass disk (Danyushevsky et al., 2011). Iron was used as the internal standard. All results were linear drift corrected and the accuracy is better than 20% for most elements (Danyushevsky et al., 2011). The detection limits are tens ppm for Fe and S, 2–5 ppm for Ti, As and Se, 0.1–1 ppm for Mo, Cd, Te and Sn, and near 0.01 ppm for other elements. The detailed methodology is described in Large et al. (2007) and Maslennikov et al. (2009).

4.3. Sulfur isotope analysis

After trace elements analysis, the representative pyrite and chalcopyrite grains on thin sections were selected for in situ sulfur analysis. In-situ sulfur isotope analyses were obtained by a Neptune Plus MC-ICP-MS equipped with a Geolas HD excimer ArF laser ablation system at the Wuhan Sample Solution Analytical Technology Co., Ltd, Hubei, China. Detailed analysis process can be found in Fu et al. (2016) and a brief description is given in this study. The laser spot size was set to 44 μm with a slow pulse frequency of 2 Hz. The fluence was kept constant at ~ 5 J/cm^2 during 100 laser pulses on sulfides. Isotopes including ^{32}S, ^{33}S, ^{34}S were collected using Faraday cups with static mode. A pyrite standard PPP-1, a chalcopyrite standard GBW07268 were analyzed to correct the matrix effect. To verify the accuracy of the analytical method, three in-house sulfides standards were also analyzed repeatedly, including a pyrrhotite SP-Po-01 ($\delta^{34}S_{v\text{-}CDT} = 1.4 \pm 0.4$), a pyrite SP-PY-01 ($\delta^{34}S_{v\text{-}CDT} = 2.0 \pm 0.5$), and a chalcopyrite SP-CP-01 ($\delta^{34}S_{v\text{-}CDT} = 5.5 \pm 0.3$). The results were corrected for instrumental mass fractionation using a standard-sample bracketing method.

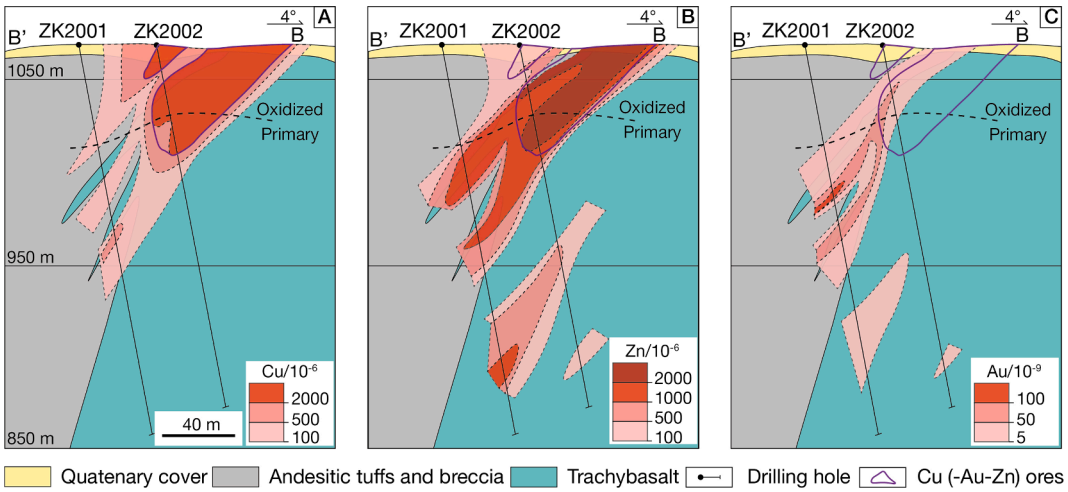

Fig. 4. Concentration zoning characteristics of Cu, Zn and Au primary halos at the cross-section B-B' of the Xiaobaliang Cu-Au deposit (modified after Zhang et al., 1991).

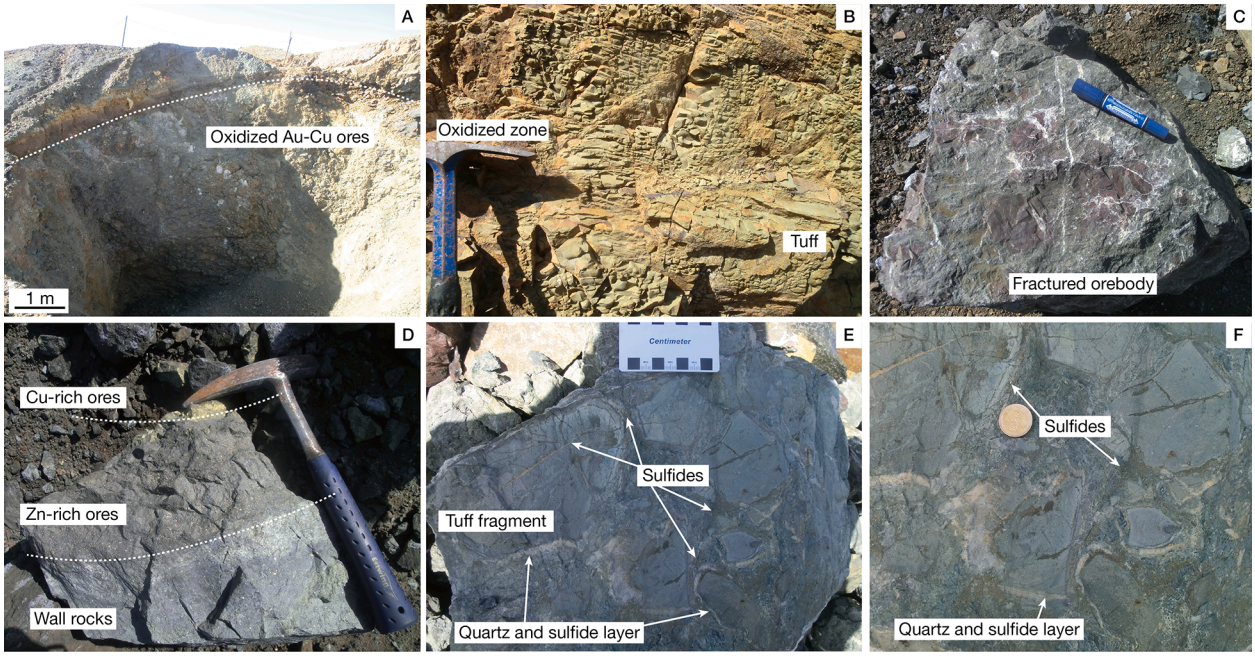

Fig. 5. Photographs of ores and wall rocks at Xiaobaliang deposit. (A-B) the figures of oxidized Au-Cu ores and surrounding andesitic tuff; (C) the fractured Cu-Au sulfide ores, with abundant hydrothermal quartz and chlorite; (D) contact between the ores and wall rocks, showing the gradual distribution of Cu-rich ores, Zn-rich ores and the wall rocks (andesitic tuff); (E-F) tuff fragments cemented by the chlorite-bearing sulfide veins. Notice that the edge of andesitic tuff is characterized by quartz veins.

5. Results

5.1. Zircon U-Pb geochronology

The results of U-Pb isotopes and U, Th, Pb contents are listed in Table 1. The zircon grains are typically 40 ~ 400 μm long and exhibit oscillatory zoning under CL (Fig. 8A). The analytical isotopes are consistent on the U-Pb isochron diagram and the common lead content is below the detection limits for most spots. After common lead calibration, twenty-one spot analyses on zircon grains from andesite tuff (XB-10) yield a concordia age of 326 ± 3 Ma (MSWD = 5.6, n = 21, Fig. 8B), which is the same as its weighted mean age (326 ± 3 Ma, n = 21). These zircon grains commonly exhibit high Th/U ratios among 0.34–0.88, with an average value of 0.68.

5.2. Sulfide compositional characters

Fifty-one sets of LA-ICP MS data were obtained for different types of pyrite and chalcopyrite from Xiaobaliang. Py2 grains are generally small in size (5–20 μm) and the matrix of the wall rocks or other kinds of sulfides were incorporated during laser ablation, thus the resulting trace element compositions of Py2 are unreliable. Fig. 9 shows the typical LA-ICP MS spectra of selected trace elements for each type of pyrite and chalcopyrite. The trace element contents of all spot analyses are provided in Table 2 and Fig. 10.

The lamellar pyrite (Py1) contains low levels of most trace elements, except for high Mn (2744–8838 ppm), V (2.22–35.3 ppm) and Ni (24.0–72.0 ppm) contents (Table 1). Py1 also has significantly high Au (1.4–10.45 ppm; average: 5.07 ppm) content, and the average Au contents in Py1 are the highest among all types of pyrite (Fig. 10A). The

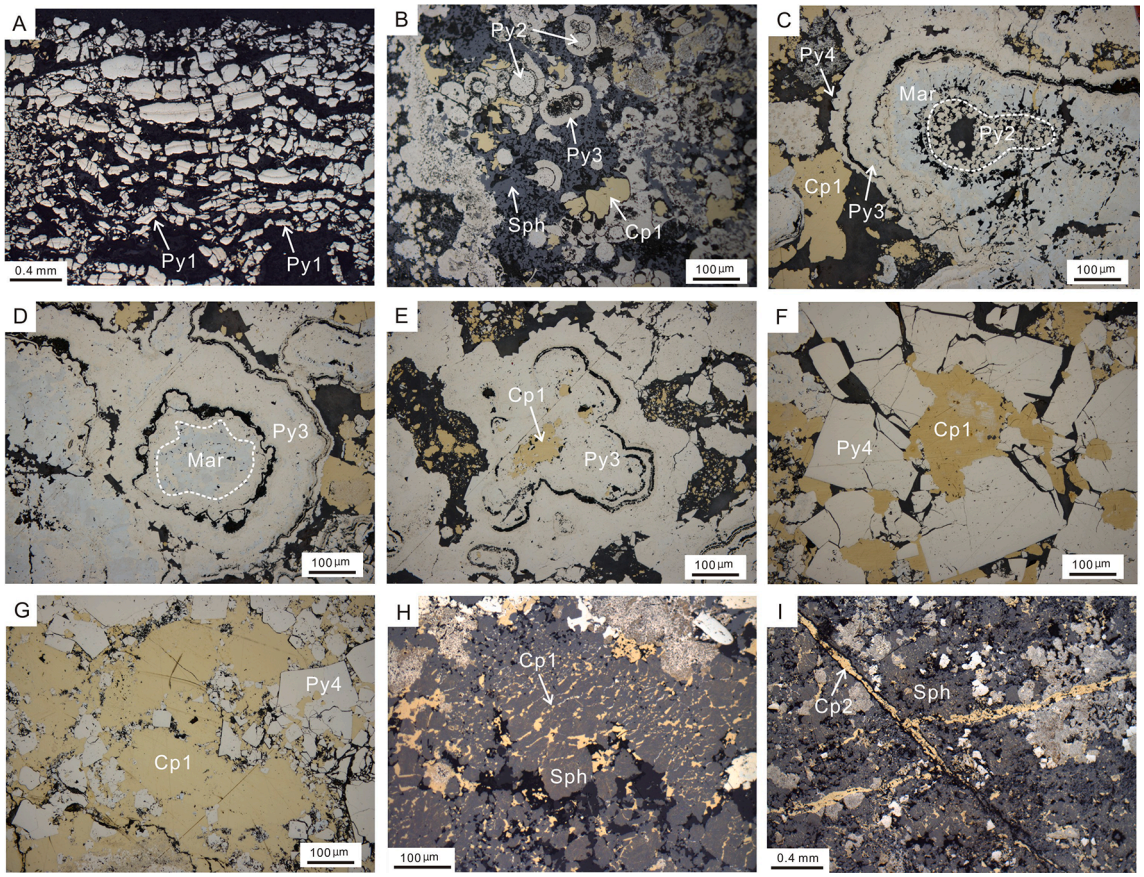

Fig. 6. Photomicrographs of mineral assemblages at the Xiaobaliang Cu-Au deposit, showing different types of pyrite and chalcopyrite. (A) lamellar pyrite (Py1) in the wall rocks; (B) framboidal pyrite (Py2) surrounded by colloidal pyrite (Py3) in the Cu-Zn ores; (C) sulfide assemblages of framboidal pyrite (Py2), marcasite (Mar), colloidal pyrite (Py3) and euhedral pyrite (Py4) in sequence from core to rim; (D) colloidal pyrite (Py3) with marcasite (Mar) core; (E) colloidal pyrite (Py3) replaced by chalcopyrite (Cp1); (F) coarser-grained euhedral pyrite (Py4) with chalcopyrite (Cp1) in fractures; (G) aggregates of chalcopyrite (Cp1) cementing euhedral pyrite (Py4); (H) sphalerite replaced by chalcopyrite, forming distinct chalcopyrite disease texture; (I) chalcopyrite veinlets (Cp2) cutting sphalerite-rich ores.

patterns for most trace elements are fairly smooth, parallel to the Fe pattern, indicating that these elements are probably contained as solid solutions in the structure of Py1 (Fig. 9A).

The colloform pyrite (Py3) contains high As (65.5–124 ppm), Zn (77.8–1136 ppm), Cd (1.11–9.81 ppm), Tl (19.2–47.9 ppm) and Pb (34.0–164 ppm). The average Zn, Cd, Tl and As contents in Py3 are the highest among all types of pyrite. The Au contents in Py3 vary from 1.60 to 3.75 ppm (average 2.84 ppm, Table 1). The marcasite in the core of Py3 has similar trace element compositions to those of Py3 except for lower Co (2.10–4.79 ppm; Table 1). In this study, marcasite is considered as Py3 due to its close association and similar chemical composition. The fluctuations of Cu and Pb spectra are probably due to the occurrence of chalcopyrite and galena micro inclusions in Py3 (Fig. 9B, C). The euhedral pyrite (Py4) in the main Cu ores has higher Co (22.4–1110 ppm), Cu (43.9–12958 ppm), Se (7.24–116 ppm) and Te (0.2–9.22 ppm) concentrations, compared to those of Py3. The extremely high concentrations of Cu might be a result of chalcopyrite micro inclusions in Py4 crystals, as revealed by several spikes of Cu in some spectra (e.g., Fig. 9D). The Co/Ni ratio of py4 is the highest among all the types of pyrite. The Au contents of Py4 range from 0.26 to 2.81 ppm (average 0.75 ppm, Table 1), lower than that of Py3.

Chalcopyrite, Cp1 is characterized by elevated Co (0.76–1064 ppm), Se (377–771 ppm) and Te (19.4–48.5 ppm). The Au contents range from 0.43 to 5.52 ppm (average 2.08 ppm; Table 1). The patterns for most elements are smooth, except for Co and Zn, which show some spikes that are caused by micro inclusions (Fig. 9E). Compared with Cp1, Cp2 shows significantly higher V (83.8–295 ppm), Mn (62.3–329 ppm), Ni (1.06–59.8 ppm), As (25.2–230 ppm) and Pb (111–684 ppm), but lower Co, Se and Te contents (Fig. 10B). The Au contents in Cp2 vary from 0.25 to 2.42 ppm (average 1.54 ppm, Table 1), slightly higher than that of Cp1. The irregular patterns of V and Mn suggest that these two elements are probably present as micro inclusions (Fig. 9F).

5.3. Sulfides isotopic features

Altogether twenty-two pyrite spots and six chalcopyrite spots were conducted for LA-MC-ICP-MS S isotope analysis and the results are shown in Table 3 and Fig. 11. Six analyses from lamellar pyrite (Py1) have yielded the variable $\delta^{34}S$ values from −30.70 ‰ to −1.50 ‰ with an average of −15.01 ‰. The framboidal pyrite grains (Py2, n = 6) exhibit the uniform $\delta^{34}S$ values of + 1.45 ‰ ~ +2.50 ‰ (average + 2.13 ‰). Similar sulfur isotopic compositions are obtained in colloform pyrites (Py3, +1.46 ‰ ~ +3.06 ‰, n = 6) and euhedral pyrites (Py4, +2.27 ‰ ~ +3.15 ‰, n = 4). As for chalcopyrite, early-stage chalcopyrite aggregates (Cp1) share the narrow $\delta^{34}S$ values of + 0.44 ‰ ~ +0.65 ‰ (average + 0.56 ‰, n = 3) whereas the chalcopyrite veinlets (Cp2) have shown the negative $\delta^{34}S$ values of −7.81 ‰ ~ −4.50 ‰ (average −5.72 ‰, n = 3).

6. Discussion

6.1. Deposition of pyrite and chalcopyrite

The LA-ICP MS analyses show that the four types of pyrite and two

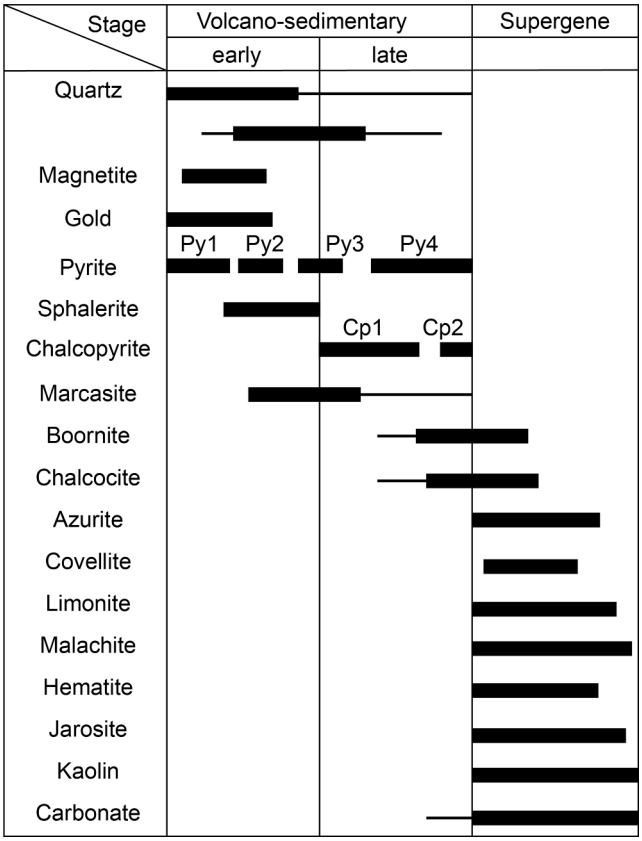

Fig. 7. Paragenetic sequence of the Xiaobaliang Cu-Au deposit.

types of chalcopyrite have distinctive trace element compositions. The distribution of trace elements in different types of sulfides depends on a complex combination of physical and chemical factors, such as temperature, pH, redox condition and element substitution capability (Oudin and Constantinou, 1984; Butler and Nesbitt, 1999; Maslennikov et al., 2009; Revan et al., 2014).

Cobalt and Ni are commonly enriched in pyrite and sensitive to the temperature variation, thus these elements can be used to reveal the deposition conditions (Bralia et al., 1979; Brill, 1989; Koglin et al., 2010). Diagenetic pyrites generally take low Co, Ni contents with low Co/Ni ratios (<1), whereas hydrothermal pyrites commonly show variable Co and Ni concentrations and have Co/Ni ratios > 1 (Bralia et al., 1979). Especially, the pyrites in volcanic rock-related deposits are characterized by high Co/Ni ratios (>10, Brill, 1989). Lamellar Py1 from the Xiaobaliang deposit has low Co and high Ni concentrations, with extremely low Co/Ni ratios of 0.27–1.52 (average 0.62). Although framboidal Py2 is too small for trace element analysis, both lamellar and framboidal textures are typical for pyrite deposited during the sedimentation process (Large et al., 2007; 2009). Many studies have shown that framboidal pyrite is the earliest pyrite in SEDEX and VHMS deposits and is commonly replaced by coarser-grained anhedral to euhedral pyrite of hydrothermal origin (e.g., Huston et al., 1992; Large, 1992; Large et al., 2007). This characteristic is also present at the Xiaobaliang deposit (Fig. 6A, B). The colloform, hydrothermal Py3 exhibits low concentrations of Co but relatively high Co/Ni ratios of 0.38–5.40 (average 2.25). This implies that Py3 precipitated from the volcanic exhalative hydrothermal fluids at a relatively lower temperature. The presence of marcasite in the core of Py3 also indicates that Py3 precipitated rapidly from low-temperature hydrothermal fluids. Meanwhile, euhedral Py4 has high Co and low Ni concentrations with elevated Co/Ni ratios of 3.51–507 (average 47.0), which is similar to that of pyrite from VHMS deposits (Fig. 12A). This suggests that Py4 formed from volcanic exhalative hydrothermal fluids at high temperatures. The high Co concentrations in pyrite are typical of high-temperature Cu-rich ores in many VHMS deposits (Huston et al., 1995; Hannington et al., 1999).

Apart from the elements like Co and Ni, Se and Sn are also sensitive to the fluid condition. Many studies on VHMS deposits and porphyry-epithermal deposits have demonstrated the enrichment of Se and Sn in pyrite at high temperature (e.g., Halbach et al., 2003; Maslennikov et al., 2009; Tanner et al., 2016). Since the substitution of S by Se in pyrite is dominated by Se^0 and/or Se^{-1}, an anoxic and acidic environment is favorable for Se incorporation (Kang et al., 2011; Diener et al., 2012). The increasing concentrations of Se and Sn in pyrite from Py1 to Py4 are consistent with increasing temperatures and decreasing oxygen fugacity of the hydrothermal fluids at Xiaobaliang (Fig. 12B). Likewise, Mn and V contents decrease significantly from Py1 to Py4 (Fig. 12C), suggesting a huge temperature increase as these elements tend to be concentrated in pyrite precipitated at low temperatures (Maslennikov et al., 2009). However, unlike Mn and V, the Tl contents in pyrite give complex information. Thallium precipitation from VHMS fluid systems is likely to be caused by the rapid oxidation of reduced sulfur and cooling of hydrothermal fluids via seawater mixing (Smith and Huston, 1992). At Xiaobaliang, Tl concentrations decrease from Py3 to Py4 (Fig. 12D), consistent with the relatively lower temperature and increasing fO_2 when Py4 precipitated. But Py1 has the lowest Tl concentrations of all the pyrites analyzed. One explanation could be that Py1 precipitated in an extremely reduced euxinic environment distal to the hydrothermal center on the seafloor. Meanwhile, the Cp1 is intergrown with Py3&Py4 and contains high concentrations of Co, Se with high Co/Ni ratios of 7.24–229 (average 91.1, Fig. 12A). On the plot of Co versus Ni, most of the Cp1 spots also fall in the field of chalcopyrite in VHMS deposits (Fig. 14A), indicating that Cp1 also precipitated from volcanic exhalative hydrothermal fluids with at temperature. In contrast, Cp2 is enriched in Mn, V, Ni and Pb with low Co/Ni ratios of 0.1–1.79 (average 0.71), suggesting its precipitation from a low-temperature hydrothermal fluid. These elemental patterns are consistent with previous fluid inclusion studies (Chen et al., 1995), where the late-stage hydrothermal fluids were homogenized around 310 ~ 350 ℃ in the quartz from Cu-rich ores. Meanwhile, the fluid inclusions from the early-stage quartz within andesitic tuff are homogenized around 260 ~ 280 ℃.

Based on the results of sulfide trace element geochemistry, we conclude that the early-stage Lamellar pyrite (Py1) from andesitic tuff, and framboidal pyrite (Py2) from Zn-rich ores formed by diagenesis in a low-temperature and extremely reduced sedimentary environment. The late-stage high temperature and reduced hydrothermal fluids have resulted in the precipitation of the coarse-grained colloform pyrite (Py3) and massive chalcopyrite (Cp1) within the footwall trachybasalt. The euhedral pyrite (Py4) and chalcopyrite veinlets (Cp2) from the fractured Cu ores formed at a relatively lower temperature and under weakly reduced conditions compared with massive Cu ores.

6.2. *Source of ore-forming metals*

In general, metals in VHMS deposits are interpreted to be derived from two possible sources: (1) leaching of basement rocks by seawater circulation (e.g., Stolz and Large, 1992; Galley, 2003; Franklin et al., 2005), and (2) direct input from magmatic-hydrothermal fluids (Sawkins and Kowalik, 1981; Yang and Scott, 2002).

Chalcopyrite is the dominant Cu-bearing mineral at Xiaobaliang. Cp1 has higher Se and Co concentrations and higher Co/Ni ratios than Cp2. Copper concentrations in pyrite increase from Py3 to Py4, and there is a positive correlation between Cu and Se (Fig. 13A). Selenium is commonly enriched in the high-temperature Cu-rich parts of many VHMS deposits and modern black smoker chimneys (e.g., Marchig et al., 1997; Hannington et al., 1999). The positive correlation of Cu and Se indicates that Cu was derived from a high-temperature fluid at Xiaobaliang. Similar trend can be also observed for Zn in pyrite (Fig. 13B). In this scenario, Cu and Zn were either leached from underlying volcanic rocks or directly sourced from magma. In situ chalcopyrite sulfur isotope

Table 1
LA-ICP-MS zircon U-Pb isotope data of andesite tuff (XBL-10) from Xiaobaliang.

Sample no.	Concentration (ppm)		Th/U	$^{207}Pb/^{206}Pb$		$^{207}Pb/^{235}U$		$^{206}Pb/^{238}U$		$^{207}Pb/^{206}Pb$		$^{207}Pb/^{235}U$		$^{206}Pb/^{238}U$		Concordance (%)
	Th	U		Ratio	2σ	Ratio	2σ	Ratio	2σ	Age (Ma)	2σ	Age (Ma)	2σ	Age (Ma)	2σ	
XBL-10–01	82.8	129	0.64	0.05382	0.00562	0.38925	0.03966	0.05246	0.00148	364	180	334	28	330	10	101
XBL-10–02	67.0	114	0.59	0.05439	0.00676	0.38264	0.04646	0.05103	0.00166	387	214	329	34	321	10	102
XBL-10–03	145	170	0.85	0.05645	0.00510	0.40575	0.03558	0.05214	0.00144	470	144	346	26	328	8	105
XBL-10–04	51.0	87.1	0.59	0.05282	0.00734	0.36410	0.04978	0.05000	0.00156	321	256	315	38	315	10	100
XBL-10–05	186	213	0.88	0.05397	0.00450	0.38162	0.03090	0.05128	0.00134	370	136	328	22	322	8	102
XBL-10–06	91.1	143	0.64	0.05605	0.00612	0.42427	0.04524	0.05490	0.00164	454	184	359	32	345	10	104
XBL-10–07	90.5	134	0.67	0.05625	0.00524	0.41906	0.03796	0.05403	0.00152	462	150	355	28	339	10	105
XBL-10–08	92.8	114	0.81	0.05276	0.00582	0.37785	0.04060	0.05194	0.00160	318	188	325	30	326	10	100
XBL-10–09	104	155	0.67	0.05441	0.00490	0.40494	0.03556	0.05398	0.00142	388	150	345	26	339	8	102
XBL-10–10	64.1	107	0.60	0.05297	0.00632	0.37690	0.04410	0.05160	0.00152	328	212	325	32	324	10	100
XBL-10–11	100	135	0.74	0.05669	0.00636	0.39304	0.04284	0.05029	0.00168	479	182	337	32	316	10	107
XBL-10–13	104	138	0.75	0.05285	0.00510	0.37971	0.03574	0.05211	0.00142	322	164	327	26	327	8	100
XBL-10–14	74.8	124	0.60	0.05251	0.00556	0.37831	0.03916	0.05226	0.00152	308	182	326	28	328	10	99
XBL-10–15	60.8	179	0.34	0.05712	0.00466	0.40852	0.03238	0.05188	0.00134	496	128	348	24	326	8	107
XBL-10–16	101	148	0.68	0.05493	0.00592	0.38646	0.04044	0.05103	0.00160	409	178	332	30	321	10	103
XBL-10–18	103	142	0.73	0.05310	0.00560	0.37274	0.03842	0.05092	0.00144	333	182	322	28	320	8	101
XBL-10–20	116	194	0.60	0.05315	0.00416	0.37960	0.02884	0.05180	0.00128	335	128	327	22	326	8	100
XBL-10–24	42.0	67.7	0.62	0.05606	0.00954	0.39401	0.06578	0.05098	0.00212	455	298	337	48	321	14	105
XBL-10–25	118	148	0.80	0.05100	0.00522	0.36016	0.03604	0.05123	0.00144	241	178	312	26	322	8	97
XBL-10–26	69.6	126	0.55	0.05275	0.00560	0.38471	0.03994	0.05290	0.00152	318	184	330	30	332	10	99
XBL-10–27	105	125	0.84	0.05430	0.00590	0.38581	0.04096	0.05153	0.00154	384	184	331	30	324	10	102

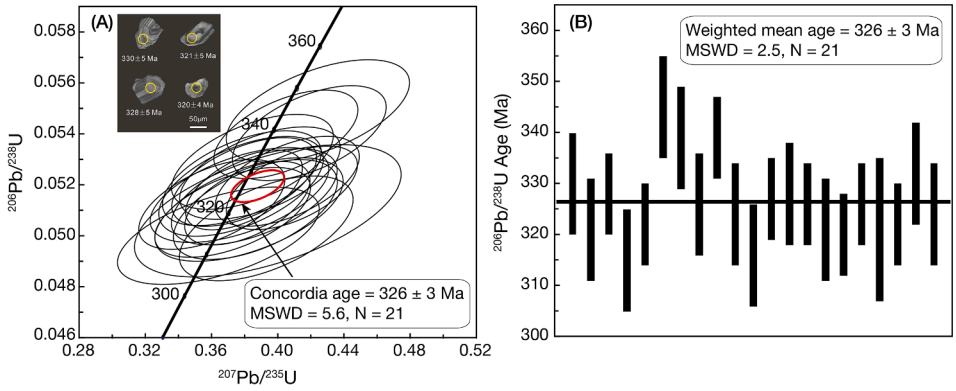

Fig. 8. The zircon U-Pb ages of andesitic rocks (XB-10) from the Xiaobaliang Cu-Au deposit.

analysis has suggested narrow $\delta^{34}S$ values in chalcopyrite from massive Cu ores (+0.44 ‰ ~ +0.65 ‰, Cp1). The chalcopyrites from later veinlets (Cp2), however, exhibit the much lower $\delta^{34}S$ values of −7.81 ‰ ~ −4.50 ‰. The Cp2 veinlets have overlapped on the massive ores and altered rocks when deposition, thus the biogenetic and ^{32}S enriched sulfur from volcanic-sedimentary sequence may have modified the fluid during the contamination. The Cp1 from massive Cu ores, on the contrary, does not exhibit such features. Moreover, the high $\delta^{18}O_{H2O}$ (5.4 ‰ – 6.1 ‰) and $\delta^{18}D_{H2O}$ values (-75 – −57 ‰) also supported that the dominant ore-forming fluids were derived from magmatic-hydrothermal fluids, rather than seawater (Chen et al., 1995). We, therefore, infer that Cu and Zn were mainly sourced from the magmatic heat source below

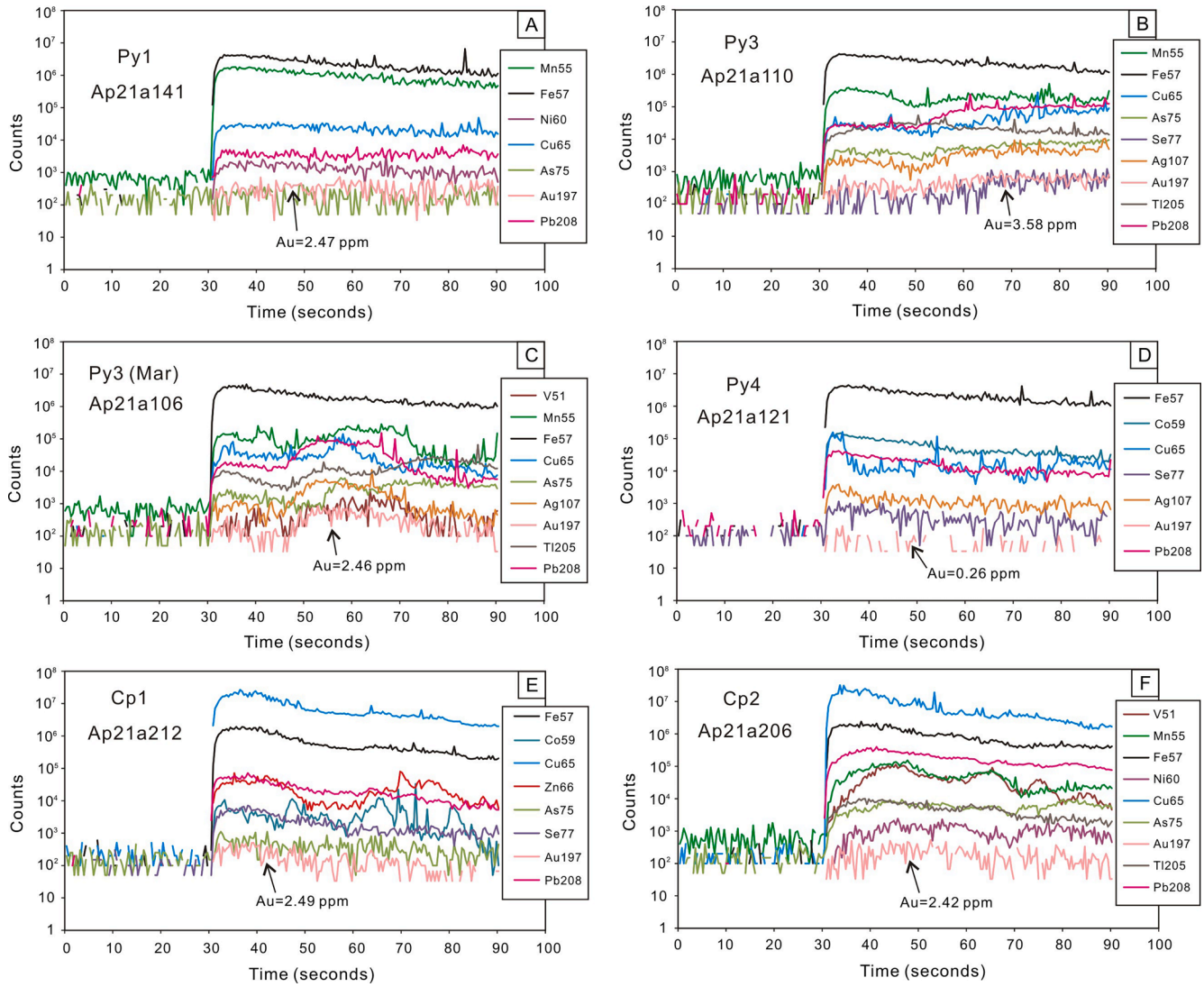

Fig. 9. Typical LA-ICP MS counts spectrum for each type of pyrite and chalcopyrite.

the feeder zone of the Xiaobaliang VHMS deposit.

Unlike Cu and Zn, the source of Au at Xiaobaliang is more complicated. Since gold was mainly concentrated in the now mined-out oxide ores, previous workers proposed that Au was enriched by the weathering of primary Cu ores (Chen et al., 1995). If this was the case, then Au would have also been derived primarily from the high-temperature magmatic-hydrothermal fluids. Since high-temperature alkaline fluids tend to transport more Te in the magmatic-hydrothermal system (Ciobanu et al., 2012; Keith et al., 2018), the progressive enrichment of Te from Py1 to Py4 is consistent with the contribution of magmatic fluids in Cu-rich ores. However, there is no positive correlation between Au and Te in different pyrite generations (Fig. 13E). The lamellar pyrite (Py1) contains the highest Au and Mn concentrations among all the types of sulfides but is depleted in Te and Ag, with its gold contents above the pyrite Au-As saturation line (Fig. 13C-F). This Au and Mn enrichment in lamellar pyrite is consistent with the previously reported Au and Mn anomalies in altered andesitic tuff (Zhang et al. 1991). This signifies that the Au was enriched in low-temperature fluids and hosted in lamellar pyrite (Py1) as mineral inclusions. Petrographic observations show that hydrothermal pyrite was replaced by Cp1, indicating that Au precipitated before the Cu mineralization. One possible explanation is that Au-bearing ores were precipitated from low-temperature hydrothermal fluids in an early stage of volcanism. Moreover, the negative sulfur isotopes from Py1 (-30.70 ‰ ~ −1.50 ‰) indicate a diagenetic origin for lamellar pyrite. This could imply that Au has a close correlation with Au-rich sediments deposited on the seafloor. It is well documented that for many VHMS deposits that formed beneath seafloor covered with sedimentary rocks, the sediments can provide a component, and in some cases may be the dominant source of ore-forming materials (Large, 1992; Franklin et al., 2005; Large et al., 2007). Therefore, we propose that at Xiaobaliang, Au was leached from the Au-rich sediments during hydrothermal convection of seawater. In addition, the ultramafic and mafic volcanic rocks in the Hegenshan area are proposed to be the products of asthenospheric upwelling/mantle-melting (Jian et al., 2012), which may have contributed to the Au enrichment in volcanic-sedimentary sequence.

6.3. Deposit type and mineralization age

Most VHMS deposits share common characteristics: (1) the ore bodies are dominantly strata-bound accumulations of sulfide minerals that precipitated at or near the seafloor, and ore is dominantly conformable with wall rocks; (2) deposits commonly consist of the concordant massive sulfide lens in the upper parts, and discordant vein-type sulfides located mainly in the footwall strata, commonly called the stringer or stockwork zone (Franklin et al., 2005); (3) deposits are polymetallic (Zn-Cu) and commonly display metal zoning in bimodal volcanic rocks, with Cu- and Fe-rich sulfides (e.g., chalcopyrite, pyrite and

Table 2
Trace element concentrations (ppm) of different types of pyrite and chalcopyrite at the Xiaobaliang Cu-Au deposit.

Sample no.	Mineral	Ti	V	Mn	Fe	Co	Ni	Cu	Zn	As	Se	Mo	Ag	Cd	Sn	Te	Au	Tl	Pb	Bi
AP21a136	Py1	8.77	25.6	8838	465,500	25.9	24.0	798	20.0	12.5	13.7	<0.13	0.35	<0.16	0.16	<0.14	10.4	0.07	44.5	0.01
AP21a137	Py1	15.3	22.4	5297	465,500	22.8	45.9	591	22.9	6.73	<5.55	<0.10	0.31	<0.11	0.12	0.16	4.45	0.10	22.1	0.01
AP21a138	Py1	349	35.3	2744	465,500	15.2	57.0	630	24.5	11.0	<4.09	<0.20	0.39	0.02	0.26	0.37	1.40	0.42	41.8	0.01
AP21a139	Py1	8.82	5.39	6062	465,500	37.1	24.4	890	19.5	4.23	8.82	<0.11	0.45	<0.16	0.12	0.18	4.27	0.19	30.4	<0.00
AP21a140	Py1	71.9	2.46	5392	465,500	23.8	28.1	828	26.5	1.43	<4.83	<0.16	0.06	0.02	<0.08	<0.32	7.09	0.01	17.9	0.03
AP21a141	Py1	76.1	2.22	3513	465,500	12.3	36.1	493	28.1	<1.07	<3.19	<0.21	0.06	0.03	<0.07	0.02	2.47	0.02	8.35	0.00
AP21a142	Py1	101	4.89	3809	465,500	18.1	47.6	685	25.0	5.67	<4.88	<0.17	0.17	0.04	<0.08	0.30	4.56	0.02	24.9	0.01
AP21a143	Py1	441	6.10	4562	465,500	52.8	72.0	686	29.9	<1.32	<4.12	<0.16	0.94	<0.07	<0.09	0.05	5.83	0.02	14.4	<0.01
	Avg.	134	13.0	5027	465,500	26.0	41.9	700	24.5	6.91	11.2		0.34	0.03	0.16	0.18	5.07	0.10	25.5	0.01
AP21a102	Py3	3.46	4.66	677	465,500	37.3	9.07	754	77.8	116	30.5	2.79	21.0	1.27	0.29	3.04	3.21	44.8	117	0.81
AP21a103	Py3	2.80	2.93	560	465,500	1.66	1.92	427	353	88.0	5.50	1.74	8.05	1.27	0.12	0.33	1.60	42.9	34.0	0.09
AP21a104	Py3	3.18	7.47	495	465,500	32.5	6.02	997	114	130	140	1.64	12.3	2.19	2.42	1.40	2.22	38.5	87.6	0.35
AP21a105	Py3	5.48	4.22	561	465,500	4.79	7.05	925	180	107	26.3	3.86	22.7	1.36	0.47	1.84	3.52	30.6	122	0.19
AP21a106	Mar	3.10	2.74	453	465,500	2.10	3.29	719	100	76.6	16.6	2.73	14.7	1.11	0.45	0.95	2.46	27.1	89.3	0.11
AP21a107	Mar	3.59	2.91	465	465,500	2.85	6.50	892	118	66.6	28.2	3.14	19.2	1.31	0.58	1.73	2.85	19.2	134	0.27
AP21a108	Mar	<2.17	2.32	520	465,500	2.34	6.18	678	102	65.5	23.4	2.58	18.6	1.14	0.48	0.90	2.84	22.7	117	0.23
AP21a109	Py3	4.76	4.37	548	465,500	4.50	9.47	924	150	92.2	31.8	4.40	27.3	2.01	1.36	1.95	3.75	26.3	164	0.33
AP21a110	Py3	2.66	4.55	724	465,500	41.2	10.0	961	157	124	38.1	2.98	23.1	1.78	0.33	3.15	3.58	38.2	163	0.86
AP21a111	Py3	3.50	3.26	279	465,500	20.7	7.23	723	1136	119	94.1	1.13	12.4	9.81	2.55	1.40	2.33	47.9	97.5	0.61
	Avg.	3.62	3.94	528	465,500	15.0	6.68	800	249	98.5	43.4	2.70	17.9	2.33	0.90	1.67	2.84	33.8	113	0.38
AP21a099	Py4	3.27	0.10	5.61	465,500	155	3.64	116	3.71	7.39	35.9	0.23	0.79	0.03	<0.08	0.20	0.50	0.35	17.1	<0.03
AP21a100	Py4	2.86	<0.09	5.37	465,500	343	5.93	195	4.80	17.7	77.0	0.31	1.37	0.27	<0.10	0.92	0.53	0.82	35.2	0.04
AP21a101	Py4	2.54	0.08	359	465,500	60.8	0.12	43.9	181	96.3	15.5	4.76	0.64	0.44	0.29	0.23	1.32	32.6	13.9	<0.01
AP21a112	Py4	<1.96	1.26	23.7	465,500	158	8.93	4127	11.5	52.6	21.6	0.37	34.8	0.52	2.39	4.33	0.63	4.68	19.6	1.24
AP21a113	Py4	4.02	0.68	10.2	465,500	242	6.84	2797	10.7	41.4	38.7	0.36	27.2	0.52	1.58	4.54	0.47	6.72	34.7	1.18
AP21a114	Py4	2.11	0.66	14.8	465,500	231	4.23	860	5.10	23.0	29.5	0.42	13.1	0.23	0.83	3.45	0.26	5.46	33.8	0.52
AP21a121	Py4	3.76	0.97	15.0	465,500	305	0.88	340	1.58	5.92	36.6	0.29	8.10	<0.15	0.53	0.87	0.26	4.34	36.3	0.09
AP21a122	Py4	1.62	0.72	19.1	465,500	335	5.49	4179	14.4	23.4	38.8	0.22	16.7	0.22	1.14	2.96	0.52	6.50	40.4	0.69
AP21a123	Py4	3.58	0.94	30.7	465,500	601	13.0	16,023	256	73.9	60.9	1.34	45.7	0.88	3.44	9.22	1.35	11.2	72.5	3.40
AP21a124	Py4	3.66	0.77	39.9	465,500	421	8.10	12,958	28.9	69.4	52.5	0.49	30.7	0.38	2.80	5.78	0.97	10.0	54.0	2.45
AP21a125	Py4	2.77	0.77	18.6	465,500	487	7.14	12,330	547	42.7	67.0	0.24	41.1	2.14	3.48	8.13	1.16	11.7	73.8	2.61
AP21a126	Py4	<2.31	0.68	13.0	465,500	807	4.26	9717	66.8	28.7	94.5	0.20	25.0	0.52	1.28	4.32	0.69	6.84	114	1.51
AP21a127	Py4	3.98	0.60	16.8	465,500	1110	5.39	6421	22.8	46.5	116	0.47	35.0	0.55	1.76	8.22	0.61	7.79	176	2.17
AP21a144	Py4	<2.96	0.21	3.21	465,500	22.4	1.21	48.3	23.1	101	10.7	7.00	0.60	<0.18	<0.09	0.25	0.28	3.82	5.06	0.03
AP21a145	Py4	2.98	2.46	16.0	465,500	88.0	25.1	41.6	6.48	19.5	9.71	7.23	0.54	0.05	0.08	<0.30	0.15	4.26	6.15	0.01
AP21a146	Py4	3.05	0.72	23.3	465,500	343	8.70	2598	423	178	39.6	4.55	5.14	1.79	0.39	1.24	0.43	6.30	61.3	0.14
AP21a147	Py4	3.70	0.26	1.98	465,500	57.4	2.12	74.0	8.74	88.9	7.24	4.76	2.14	0.30	0.17	0.61	0.55	2.22	6.72	0.31
AP21a148	Py4	3.65	1.58	120	465,500	446	21.1	9051	108	415	48.4	17.6	10.3	1.51	1.04	2.95	2.81	19.7	55.9	1.90
	Avg.	3.17	0.79	40.9	465,500	345	7.34	4551	95.8	73.9	44.5	2.82	16.6	0.65	1.41	3.42	0.75	8.07	47.6	1.14
AP21a195	Cp1	<1.95	0.32	3.36	304,300	1064	6.98	355,073	1035	7.39	442	0.29	7.68	17.7	0.97	21.0	0.43	3.64	31.1	0.20
AP21a196	Cp1	2.90	0.70	36.8	304,300	1041	4.54	268,152	732	45.9	633	0.49	50.7	15.0	1.72	48.5	5.52	28.3	327	2.27
AP21a208	Cp1	<4.39	<0.16	2.01	304,300	94.9	0.88	352,389	752	9.30	771	1.98	13.7	8.82	8.93	38.0	1.21	7.11	54.6	2.12
AP21a209	Cp1	3.06	<0.10	2.26	304,300	34.0	0.63	384,599	767	10.1	671	1.50	16.6	11.8	9.59	33.7	1.32	9.79	66.2	2.34
AP21a210	Cp1	2.92	<0.11	2.89	304,300	213	4.00	367,668	2804	26.4	544	2.83	25.6	24.8	9.29	41.6	2.05	13.6	95.2	4.76
AP21a211	Cp1	5.59	<0.21	<1.19	304,300	0.76	0.11	359,673	791	2.59	630	3.58	9.63	8.88	10.9	37.5	0.74	3.55	26.9	0.79
AP21a212	Cp1	4.19	<0.13	4.65	304,300	46.4	1.04	366,112	1265	12.7	599	5.88	25.2	15.3	8.72	24.9	2.49	20.4	110	3.63
AP21a213	Cp1	<3.99	0.48	49.2	304,300	160	6.11	299,991	1773	103	377	7.73	22.3	19.3	11.3	18.8	2.20	19.5	100	3.59
AP21a214	Cp1	3.22	0.19	11.8	304,300	156	1.86	348,112	711	19.4	431	2.53	16.5	8.82	8.54	19.4	1.11	11.9	73.0	1.67
	Avg.	3.65	0.46	15.7	304,300	218	2.39	343,337	1199	28.7	582	3.31	22.5	14.1	8.62	32.8	2.08	14.3	107	2.65
AP21a198	Cp2	6.94	168	62.3	304,300	1.81	1.06	370,279	11,190	25.2	390	0.08	12.3	6.93	24.9	0.95	0.25	1.67	111	1.34
AP21a203	Cp2	20.4	83.8	63.0	304,300	11.8	23.2	150,195	285	135	234	2.10	14.2	0.40	8.80	3.64	1.19	1.80	159	1.44
AP21a204	Cp2	3.87	208	62.8	304,300	6.07	59.8	343,334	127	134	60.0	0.40	40.8	1.45	13.5	2.68	1.43	6.02	363	2.77
AP21a206	Cp2	88.9	295	329	304,300	23.2	50.8	247,061	2251	230	196	1.25	59.9	2.68	13.4	8.99	2.42	14.0	684	4.89
AP21a207	Cp2	91.1	117	217	304,300	88.0	49.1	228,827	846	225	185	0.75	49.6	1.78	10.6	9.06	2.40	10.3	555	5.33
	Avg.	42.2	174	147	304,300	26.2	36.8	267,939	2940	150	213	0.92	35.4	2.65	14.2	5.06	1.54	6.76	374	3.15

Abbreviations: Py = pyrite, Mar = Marcasite, Cp = Chalcopyrite; Avg. = average content of trace element.

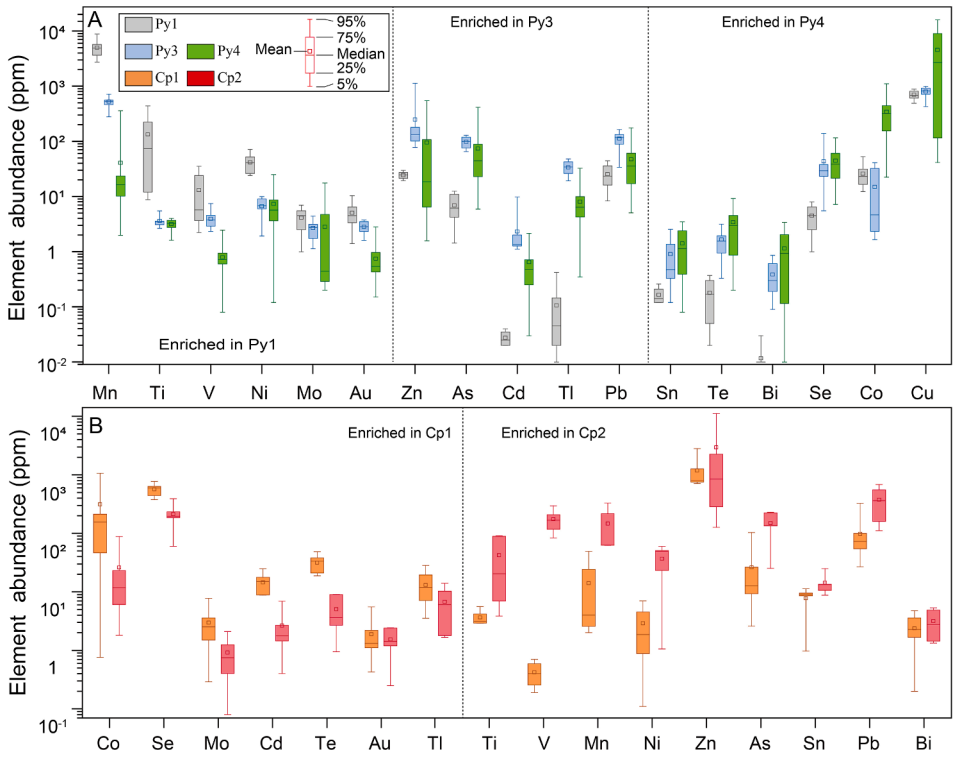

Fig. 10. Box-plots showing the concentrations (ppm) of selected trace elements from various types of pyrite and chalcopyrite at Xiaobaliang analyzed by LA-ICP MS. (A) comparison of the trace element contents for the three types of pyrite; (B) comparison of the trace element contents for the two types of chalcopyrite.

Table 3
In situ sulfur isotope analyses of pyrite and chalcopyrite at the Xiaobaliang Cu-Au deposit.

Sample No.	Type	$\delta^{33}S_{V\text{-}CDT}$(‰)	2SE	Sample No.	Type	$\delta^{34}S_{V\text{-}CDT}$(‰)	2SE
XBL11-01	Py1	−30.70	0.08	XBL4-03	Py3	3.38	0.05
XBL11-02	Py1	−25.99	0.09	XBL6-04	Py3	5.38	0.06
XBL16-01	Py1	−15.73	0.08	XBL6-05	Py3	4.20	0.06
XBL16-02	Py1	−4.88	0.08	XBL6-06	Py3	4.30	0.07
XBL16-03	Py1	−3.36	0.06	XBL20-01	Py4	5.86	0.10
XBL16-04	Py1	−9.42	0.06	XBL20-02	Py4	4.40	0.06
XBL6-01	Py2	4.24	0.04	XBL20-03	Py4	5.53	0.06
XBL6-02	Py2	4.66	0.05	XBL20-04	Py4	5.91	0.06
XBL6-03	Py2	3.36	0.05	XBL4-01	Cp1	0.59	0.07
XBL6-07	Py2	3.51	0.06	XBL4-02	Cp1	0.65	0.08
XBL6-08	Py2	3.85	0.06	XBL4-03	Cp1	0.44	0.09
XBL6-09	Py2	4.25	0.06	XBL20-01	Cp2	−7.81	0.12
XBL4-01	Py3	4.75	0.05	XBL20-02	Cp2	−4.86	0.09
XBL4-02	Py3	5.72	0.05	XBL20-03	Cp2	−4.50	0.09

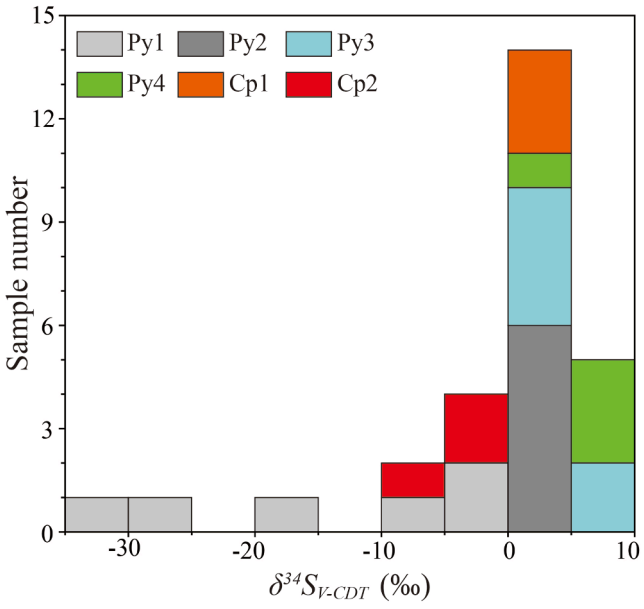

Fig. 11. $\delta^{34}S$ values of different pyrite and chalcopyrite generations in Xiaobaliang Cu-Au deposit.

pyrrhotite) being most abundant in the interiors and the underlying stockwork zones of the deposits, and Zn-rich sulfides (e.g., sphalerite) deposited near the upper margins (Hannington, 2013). In addition, ore-forming fluids of the VHMS deposit are proposed to be derived from the heated seawater that has interacted with the volcanic host rocks or released directly from the subvolcanic intrusion by magma degassing (Franklin et al., 2005).

As for the Xiaobaliang Cu-(Zn)-Au deposit, the orebodies are conformable to the host rocks and appear to be strata-bound (Fig. 3). The wall rocks are mainly andesitic tuff, tuffaceous sandstone and trachybasalt, with some rounded andesitic-basaltic fragments. These fragments are similar to pillow lava erupted on the seafloor and surrounded by sulfides with strong hydrothermal alteration, suggesting that these wall rocks were formed on the seafloor in a volcanic exhalative hydrothermal system (Fig. 5A). In the transition zone between the ores and wall rocks, there is an apparent metal zonation pattern of Cu-rich ores

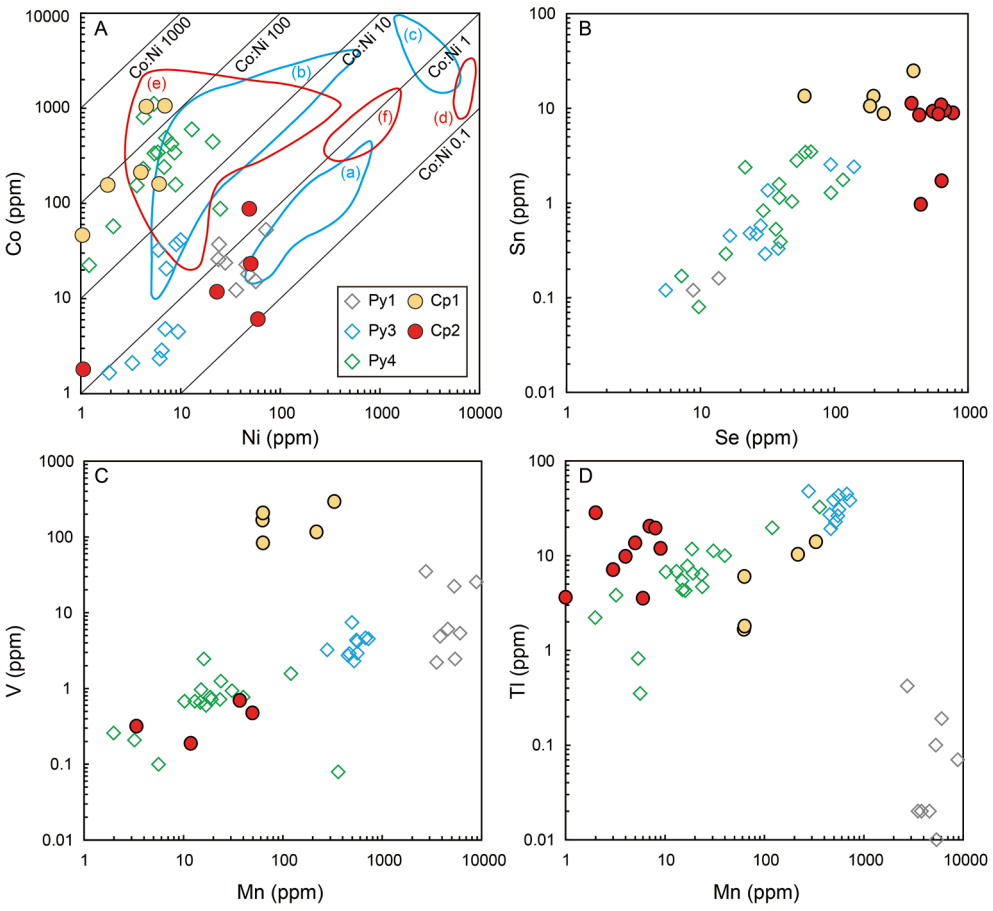

Fig. 12. Binary plots of Co vs. Ni (A), Sn vs. Se (B), V vs. Mn (C) and Tl vs Mn (D) analyzed by LA-ICP MS for different types of pyrite and chalcopyrite. The fields of pyrite and chalcopyrite in VHMS, magmatic and sedimentary deposits are cited from Bajwah et al. (1987) and Brill (1989). (a)- pyrite in sedimentary deposits; (b)- pyrite in VHMS deposits; (c)- pyrite in magmatic deposits; (d)- chalcopyrite in sedimentary deposits; (e)- chalcopyrite in VHMS deposit; (f)- chalcopyrite in magmatic deposits.

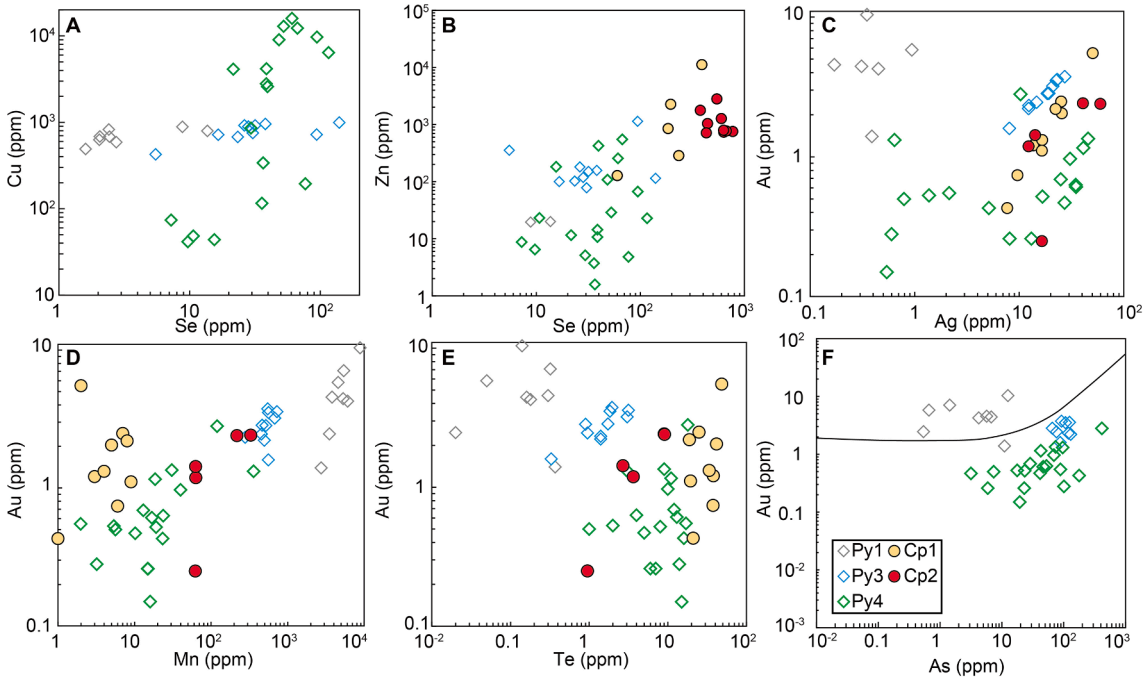

Fig. 13. Correlation between Cu-Se (A), Zn-Se (B), Au-Ag (C), Au-Mn (D), Au-Te (E) and Au-As (F) for different types of sulfides. The Au-As saturation line was after (Reich et al., 2005).

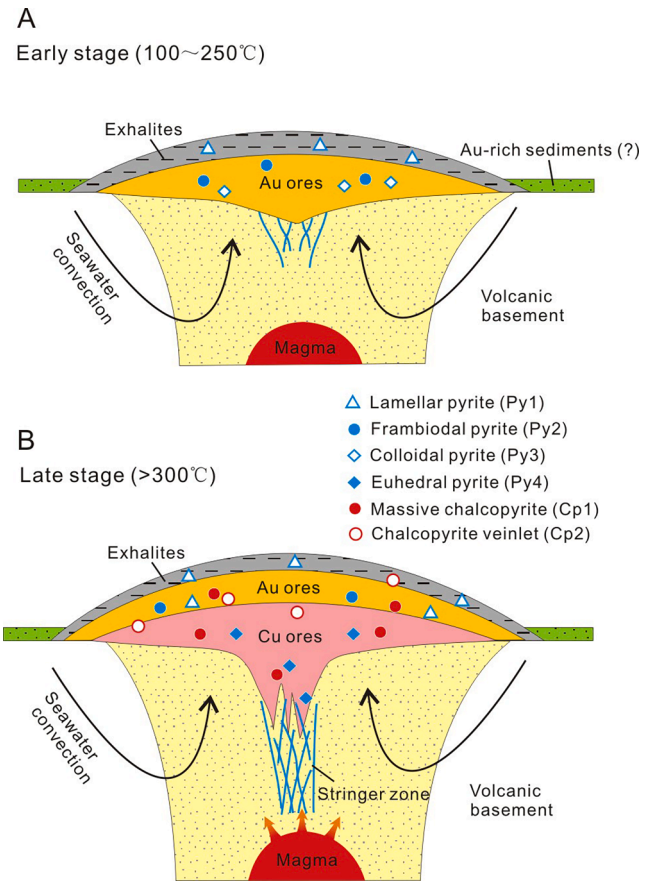

Fig. 14. Genetic model showing the two stages of mineralization at the Xiaobaliang Cu-Au deposit. (A) The early stage of mineralization occurred under relatively lower temperature conditions, gold was released from Au-rich sediments by seawater convection, forming the gold ores; (B) In the late stage of mineralization under higher temperature conditions, significant amounts of copper were dissolved in the hydrothermal fluids, forming the copper ores beneath the gold ores.

gradually changing to Zn-rich ores (Fig. 5B). This metal zoning characteristic is similar to that of the VHMS deposit with Cu mineralization occurring dominantly at the lower part of the orebody and Zn mineralization at the top and outer margins (Lydon, 1984; Franklin et al., 2005; Hannington, 2013). In terms of mineral petrographic observations, many pyrites display colloform, framboidal or concentric texture, which are also commonly present in many VHMS deposits. Both Py1 and Py2 are texturally similar to syngenetic or *syn*-diagenetic pyrite that is common in sedimentary exhalative (SEDEX) Zn-Pb-Ag deposits and Au deposits hosted in sedimentary rocks (e.g., Croxford and Jephcott, 1972; Large et al., 2007; Large et al., 2009). Sulfide trace element geochemistry also indicates that all the different types of pyrite and chalcopyrite were formed in the volcanic exhalative hydrothermal system. These geological features, volcanic rocks textures, metal zoning and sulfide geochemistry all suggest a VHMS mineralization system in the Xiaobaliang Cu-Au deposit.

As for hydrothermal minerals from altered andesitic tuff in Xiaobaliang, the pyrites are of lamellar shape (Py1) and disseminated within the fragment or pyroclastic cement (Fig. 5E-F). Quartz typically forms as clustered veins around the fragment and was cemented by the lateral volcanic components. Meanwhile, the Cu-Au sulfide ores from the Xiaobaliang deposit were hosted by the volcanic tuff. No alteration or mineralization was observed in the intrusive rocks like gabbro and quartz-keratophyre. All these features share the characteristic of volcanic exhalative hydrothermal origin and the Xiaobaliang Cu-Au deposit was deposited at the same time or slightly later than the hosted volcanic tuff. The U-Pb dating of andesitic tuff (XB-10) has yielded a weighted average age of 326 ± 3 Ma (n = 21, Fig. 8). Meanwhile, Jian et al. (2012) reported the age of 333 ± 4 Ma for plagiogranite from the Xiaobaliang area, whereas the tuff from the Hegenshan area has yielded the age of 323 ± 3 Ma (Huang et al., 2016). Lateral intrusives rocks such as unaltered gabbro were emplaced during the Mesozoic era (Huang et al., 2021). All these geochronology studies demonstrated the Late Carboniferous magmatic and related Cu-Au mineralization event around 326 Ma.

6.4. *Mineralization process and tectonic implication*

Based on the trace element data and sulfide paragenesis, the ore-forming processes at the Xiaobaliang Cu-Au deposit can be divided into two stages: early Au mineralization and late Cu mineralization. The preferred genetic model for the mineralization process is summarized in Fig. 14 and discussed below.

Early mafic volcanism and sedimentary rocks in the Xiaobaliang area have concentrated high contents of gold on the seafloor. When the subvolcanic intrusion was initially emplaced in the deep level, the rising of temperature has facilitated the low-temperature (<280 °C) seawater convection beneath the seafloor. Gold was leached from volcano-sedimentary sequence and finally precipitated in the hydrothermal exhalative sediments, together with lamellar and framboidal pyrites (Fig. 14A). Some sphalerite and marcasite were also precipitated in this stage due to the lower temperature. Later shallow emplacement of intrusions then significantly released Cu from the basement volcanics or directly supplied Cu through magma degassing (>310 °C). Chalcopyrite (Cp1), colloform (Py3) and euhedral pyrites (Py4) in the massive Cu ores then precipitated beneath the Au-rich exhalites (Fig. 14B). As the magmatic-hydrothermal system waned and the fluids got cooler, late-stage chalcopyrite veinlets (Cp2) formed, cutting across early sphalerite and filling fractures in the overlying wall rocks.

The occurrence of VHMS deposits typically suggests an extensional environment (e.g., mid-ocean ridge, submarine arc, or back-arc basin; Lydon, 1984; Large, 1992; Franklin et al., 2005; Hannington, 2013). The volcanic rocks from the Xiaobaliang area can be identified two categories: Early Carboniferous to Permian era mafic and ultramafic rocks (Robinson et al., 1999; Jian et al., 2012; Jiang and Zhu, 2019); Late Carboniferous to Permian felsic rocks (Miao et al., 2008; Wang et al., 2020). Although there are many opinions on whether the ultramafic/mafic rocks in Hegenshan-Chaogenshan belong to the part of the ophiolite belt, our studies definitely proved that a limited extension process had developed in the Early Carboniferous era. According to the summaries by Franklin et al. (2005) and Piercey (2011), felsic volcanics associated with VHMS systems typically take high Zn and Pb contents. These metal assemblages are typical for VHMS deposits from evolved continental arc to back-arc environments. However, the Xiaobaliang gold deposit is dominated by Cu-Au ores with minor Zn enrichment, which demonstrates the contribution of mafic rocks during mineralization. Therefore, we propose that the Xiaobaliang Cu-Au deposit belongs to a Cyprus-type VHMS deposit formed in the extensional environment. The Late Carboniferous upwelling of the asthenosphere mantle has resulted in the VHMS-type mineralization along the Hegenshan-Chaogenshan area.

7. Conclusions

(1) Four types of pyrite are identified in the Xiaobaliang Cu-Au deposit, including lamellar (Py1), framboidal (Py2), colloform (Py3) and euhedral pyrite (Py4). Chalcopyrite is divided into two types, consisting of early massive chalcopyrite aggregates (Cp1) and late chalcopyrite veinlets (Cp2). Based on the alteration features and ore textures of the deposit, we identify it as a VHMS deposit.

(2) Py1 and Py2 were formed by diagenesis in a sedimentary environment. Py3 and Cp1 precipitated from high-temperature volcanic exhalative hydrothermal fluids under extremely reduced conditions. Py4 and Cp2 precipitated from the hydrothermal fluids at a lower temperature under weakly reduced conditions.
(3) Trace element analyses of pyrite and chalcopyrite reveal that the Cu was derived from a magmatic-hydrothermal fluid whereas Au was probably released from Au-rich sediments by seawater leaching.
(4) Two stages of mineralization formed the Xiaobaliang Cu-Au deposit. Au was released from sediments and concentrated in the early-stage low-temperature hydrothermal fluids, forming gold ores in the upper exhalites. With the temperature progressively increasing to the late stage, significant amounts of Cu were dissolved in the magmatic-hydrothermal fluids and eventually precipitated as the main copper ores beneath the gold ores.
(5) The Cu-dominated and intermediate-mafic rocks hosted Xiaobaliang deposit belongs to the Cyprus-type VHMS deposit formed in the Late Carboniferous extensional environment.

Declaration of Competing Interest

The authors declare that they have no known competing financial interests or personal relationships that could have appeared to influence the work reported in this paper.

Acknowledgements

The authors are grateful to Paul Olin for his help with LA-ICP MS analysis. Jing Zhang is acknowledged for valuable suggestions. Detailed modifications by David R. Cooke substantially improved an early draft. Our thanks to Jun Zhong for thoughtful discussions. Qiuyue Huang is thanked for English language editing. This study was supported by the National Key Research and Development Project of China (2017YFC0601302), the National Natural Science Foundation of China (42073037, 41672067), and the Major State Basic Research Program of the People's Republic of China (2013CB429800).

References

Andersen, T., 2002. Correction of common lead in U-Pb analyses that do not report Pb-204. Chem. Geol. 192, 59–79. https://doi.org/10.1016/s0009-2541(02)00195-x.
Badarch, G., Dickson Cunningham, W., Windley, B.F., 2002. A new terrane subdivision for Mongolia: implications for the Phanerozoic crustal growth of Central Asia. J. Asian Earth Sci. 21 (1), 87–110. https://doi.org/10.1016/S1367-9120(02)00017-2.
Bajwah, Z.U., Seccombe, P.K., Offler, R., 1987. Trace-element distribution, Co-Ni ratios and genesis of the Big Cadia iron-copper deposit, New South Wales, Australia. Miner. Depos. 22, 292–300. https://doi.org/10.1007/BF00204522.
Bralia, A., Sabatini, G., Troja, F., 1979. A revaluation of the Co/Ni ratio in pyrite as geochemical tool in ore genesis problems. Miner. Depos. 14, 353–374. https://doi.org/10.1007/BF00206365.
Brill, B.A., 1989. Trace-element contents and partitioning of elements in ore minerals from the CSA Cu-Pb-Zn Deposit, Australia, and implications for ore genesis. Can. Mineral. 27, 263–274.
Butler, I.B., Nesbitt, R.W., 1999. Trace element distributions in the chalcopyrite wall of a black smoker chimney: insights from laser ablation inductively coupled plasma mass spectrometry (LA–ICP–MS). Earth Planet. Sc. Lett. 167 (3–4), 335–345. https://doi.org/10.1016/S0012-821X(99)00038-2.
Chen, B., Jahn, B.-M., Wilde, S., Xu, B., 2000. Two contrasting paleozoic magmatic belts in northern Inner Mongolia, China: petrogenesis and tectonic implications. Tectonophysics 328 (1-2), 157–182. https://doi.org/10.1016/S0040-1951(00)00182-7.
Chen, D.Q., Zhao, P., Wei, Z.G., 1995. On the submarine volcanic hydrothermal genesis of the xiaobaliang copper deposit. Acta Geosci. Sin. 190–203 (in Chinese with English abstract).
Ciobanu, C.L., Cook, N.J., Utsunomiya, S., Kogagwa, M., Green, L., Gilbert, S., Wade, B., 2012. Gold-telluride nanoparticles revealed in arsenic-free pyrite. Am. Mineral. 97 (8-9), 1515–1518. https://doi.org/10.2138/am.2012.4207.
Cook, N.J., Ciobanu, C.L., Pring, A., Skinner, W., Shimizu, M., Danyushevsky, L., Saini-Eidukat, B., Melcher, F., 2009. Trace and minor elements in sphalerite: A LA-ICPMS study. Geochim. Cosmochim. Ac. 73 (16), 4761–4791. https://doi.org/10.1016/j.gca.2009.05.045.
Croxford, N.J.W., Jephcott, S.J., 1972. The McArthur lead-zinc-silver deposit, N.T. Austral. Inst. Min. Metall. Proc. 243, 1–26.
Danyushevsky, L., Robinson, P., Gilbert, S., Norman, M., Large, R., McGoldrick, P., Shelley, M., 2011. Routine quantitative multi-element analysis of sulphide minerals by laser ablation ICP-MS: Standard development and consideration of matrix effects. Geochem-Explor. Env. A. 11 (1), 51–60. https://doi.org/10.1144/1467-7873/09-244.
Diener, A., Neumann, T., Kramar, U., Schild, D., 2012. Structure of selenium incorporated in pyrite and mackinawite as determined by XAFS analyses. J. Contam. Hydrol. 133, 30–39. https://doi.org/10.1016/j.jconhyd.2012.03.003.
Domeier, M., Torsvik, T.H., 2014. Plate tectonics in the late Paleozoic. Geosci. Front. 5 (3), 303–350. https://doi.org/10.1016/j.gsf.2014.01.002.
Franklin, J.M., Gibson, H.L., Galley, A.G., Jonasson, I.R., 2005. Volcanogenic massive sulfide Deposits. In: Hedenquist, J.W., Thompson, J.F.H., Goldfarb, R.J., Richards, J. P. (Eds.), Economic Geology 100th Anniversary Volume. Society of Economic Geologists, Littleton, CO, pp. 523–560.
Fu, J., Hu, Z., Zhang, W., Yang, L.u., Liu, Y., Li, M., Zong, K., Gao, S., Hu, S., 2016. In situ sulfur isotopes (δ34S and δ33S) analyses in sulfides and elemental sulfur using high sensitivity cones combined with the addition of nitrogen by laser ablation MC-ICP-MS. Anal. Chim. Acta 911, 14–26. https://doi.org/10.1016/j.aca.2016.01.026.
Galley, A.G., 2003. Composite synvolcanic intrusions associated with Precambrian VMS-related hydrothermal systems. Miner. Depos. 38 (4), 443–473. https://doi.org/10.1007/s00126-002-0300-9.
Galley, A.G., Hannington, M.D., Jonasson, I.R., 2007. Volcanogenic massive sulphide deposits. In: Goodfellow, W.D. (Ed.), Mineral Deposits of Canada: A Synthesis of Major Deposit-Types, District Metallogeny, the Evolution of Geological Provinces, and Exploration Methods. Geological Association of Canada, Special Publication, Mineral Deposits Division, pp. 141–161.
Gao, Z.X., 2019. Polymetallic mineralization and prospecting direction in the Gaoerqi-Chaobuleng area, Inner Mongolia (Ph. D. thesis). China University of Geosciences, Wuhan, China.
Gibson, H.L., 2005. Volcanic-hosted ore deposits. In: Marti, J., Ernst, G.G.J. (Eds.), Volcanoes in the Environment. Cambridge University Press, New York, NY, USA, pp. 332–386.
Gong, P., 2012. The types and metallogenesis of basic-ultrabasic rocks from Hegenshan area in Inner Mongolia (Master degree thesis). Jilin University. 78, pp.
Halbach, P.E., Fouquet, Y., Herzig, P., 2003. Mineralization and compositional patterns in deep-sea hydrothermal systems. In: Halbach, P.E., Tunnicliffe, V., Hein, J.R. (Eds.), Energy and Mass Transfer in Marine Hydrothermal Systems. Dahlem University Press, Berlin, pp. 85–122.
Hannington, M.D., 2013. Volcanogenic massive sulfide deposits. In: Scott, S.D. (Ed.), Geochemistry of Mineral Deposits, Treatise on Geochemistry, 13 p. 463-488.
Hannington, M.D., Bleeker, W., Kjarsgaard, I., 1999. Sulfide Mineralogy, Geochemistry, and Ore Genesis of the Kidd Creek Deposit: Part I. North, Central, and South Orebodies*. The Giant Kidd Creek Volcanogenic Massive Sulfide Deposit, Western Abitibi Subprovince, Canada 10. https://doi.org/10.5382/Mono.10.07.
Huang, B., Fu, D., Li, S., Ge, M., Zhou, W., 2016. The age and tectonic implications of the Hegenshan ophiolite in Inner Mongolia. Acta Petrol. Sin. 32 (1), 158–176 (in Chinese with English abstract).
Huang, B., Fu, D., Zhou, W., Ning, W., 2021. Complexity of zircon ages of mafic rocks in ophiolitic mélanges: A case from the Hegenshan ophiolite, Inner Mongolia. Chin. J. Geol. 56 (2), 596–614. https://doi.org/10.12017/dzkx.2021.030.
Huston, D.L., Bottrill, R.S., Creelman, R.A., Zaw, K., Ramsden, T.R., Rand, S.W., et al., 1992. Geologic and geochemical controls on the mineralogy and grain-size of gold-bearing phases, eastern Australian volcanic-hosted massive sulfide deposits. Geol. Bull. Soc. Econ. Geologist. 87, 542–563. https://doi.org/10.2113/gsecongeo.87.3.542.
Huston, D.L., Sie, S.H., Suter, G.F., Cooke, D.R., Both, R.A., 1995. Trace-elements in sulfide minerals from eastern Australian volcanic-hosted massive sulfide deposits .1. proton microprobe analyses of pyrite, chalcopyrite, and sphalerite, and .2. selenium levels in pyrite - comparison with delta-S-34 values and implications for the source of sulfur in volcanogenic hydrothermal systems. Geol. Bull. Soc. Econ. Geologist. 90, 1167–1196. https://doi.org/10.2113/gsecongeo.90.5.1167.
Jahn, B.M., 2004. The Central Asian Orogenic Belt and growth of the continental crust in the Phanerozoic. In: Malpas J., Fletcher C. J. N., Ali J. R., Aitchison J. C., editors. Aspects of the tectonic evolution of China. London: Geological Society, London, Special Publications. p. 73-100.
Jian, P., Kröner, A., Windley, B.F., Shi, Y., Zhang, W., Zhang, L., Yang, W., 2012. Carboniferous and Cretaceous mafic–ultramafic massifs in Inner Mongolia (China): A SHRIMP zircon and geochemical study of the previously presumed integral "Hegenshan ophiolite". Lithos 142-143, 48–66. https://doi.org/10.1016/j.lithos.2012.03.007.
Jiang, J., Zhu, Y., 2019. Harzburgite found in the Hegenshan ophiolite, southeastern Central Asian Orogenic Belt: Petrogenesis and geological implications. Gondwana Res. 75, 28–46. https://doi.org/10.1016/j.gr.2019.03.021.
Jiang, S.H., Zhang, L.L., Liu, Y.F., Liu, C.H., Kang, H., Wang, F.X., 2018. Metallogeny of Xing-Meng Orogenic Belt and some related problems. Mineral Depos. 37, 671–711 (in Chinese with English abstract).
Kang, M., Chen, F., Wu, S., Yang, Y., Bruggeman, C., Charlet, L., 2011. Effect of pH on Aqueous Se(IV) Reduction by Pyrite. Environ. Sci. Technol. 45 (7), 2704–2710. https://doi.org/10.1021/es1033553.
Keith, M., Smith, D.J., Jenkin, G.R.T., Holwell, D.A., Dye, M.D., 2018. A review of Te and Se systematics in hydrothermal pyrite from precious metal deposits: Insights into ore-forming processes. Ore Geol. Rev. 96, 269–282. https://doi.org/10.1016/j.oregeorev.2017.07.023.

Koglin, N., Frimmel, H.E., Lawrie-Minter, W.E., Brätz, H., 2010. Trace-element characteristics of different pyrite types in Mesoarchaean to Palaeoproterozoic placer deposits. Miner. Deposita 45 (3), 259–280. https://doi.org/10.1007/s00126-009-0272-0.

Kröner, A., Kovach, V., Belousova, E., Hegner, E., Armstrong, R., Dolgopolova, A., Seltmann, R., Alexeiev, D.V., Hoffmann, J.E., Wong, J., Sun, M., Cai, K., Wang, T., Tong, Y., Wilde, S.A., Degtyarev, K.E., Rytsk, E., 2014. Reassessment of continental growth during the accretionary history of the Central Asian Orogenic Belt. Gondwana Res. 25 (1), 103–125. https://doi.org/10.1016/j.gr.2012.12.023.

Large, R.R., 1992. Australian volcanic-hosted massive sulfide deposits; features, styles, and genetic models. Econ. Geol. 87, 471–510. https://doi.org/10.2113/gsecongeo.87.3.471.

Large, R.R., Danyushevsky, L., Hollit, C., Maslennikov, V., Meffre, S., Gilbert, S., Bull, S., Scott, R., Emsbo, P., Thomas, H., Singh, B., Foster, J., 2009. Gold and trace element zonation in pyrite using a laser imaging technique: implications for the timing of gold in orogenic and carlin-style sediment-hosted deposits. Econ. Geol. 104 (5), 635–668. https://doi.org/10.2113/gsecongeo.104.5.635.

Large, R.R., Maslennikov, V.V., Robert, F., Danyushevsky, L.V., Chang, Z., 2007. Multistage sedimentary and metamorphic origin of pyrite and gold in the Giant Sukhoi Log Deposit, Lena Gold Province. Russia. Econ. Geol. 102 (7), 1233–1267. https://doi.org/10.2113/gsecongeo.102.7.1233.

Li, W., Zhang, F., Hu, C., Zhang, L., Qiao, X., 2021. Ore genesis and tectonic setting of the Bieluwutu Cu-Pb-Zn volcanogenic massive sulfide deposit in Xing'an-Mongolia orogenic belt, China. Ore Geol. Rev. 130, 103951. https://doi.org/10.1016/j.oregeorev.2020.103951.

Liu, Y.F., Nie, F.J., Jiang, S.H., Hou, W.R., Liang, Q.L., Zhang, K., et al., 2012. Geochronology of Zhunsujihua molybdenum deposit in Sonid Left Banner, Inner Mongolia, and its geological significance. Mineral Depos. 31, 119–128 (in Chinese with English abstract.).

Longerich, H.P., Jackson, S.E., Gunther, D., 1996. Laser ablation inductively coupled plasma mass spectrometric transient signal data acquisition and analyte concentration calculation. J. Anal. At. Spectrom. 11, 899–904. https://doi.org/10.1039/ja9961100899.

Ludwig, K.R., 2003. ISOPLOT 3.00: A Geochronological Toolkit for Microsoft Excel (Berkeley Geochronology Center, Berkeley, California). Berkeley: BGC Special Publication, 1a.

Lydon, J.W., 1984. Ore Deposit Models - 8. Volcanogenic Massive Sulphide Deposits Part I: A Descriptive Model. Geosci. Can. 11, 195–202.

Marchig, V., Blum, N., Roonwal, G., 1997. Massive sulfide chimneys from the East Pacific Rise at 7°24'S and 16°43'S. Mar Georesources Geotechnol. 15 (1), 49–66. https://doi.org/10.1080/10641199709379934.

Martin, W., Baross, J., Kelley, D., Russell, M.J., 2008. Hydrothermal vents and the origin of life. Nat. Rev. Microbiol. 6, 805–814. https://doi.org/10.1038/nrmicro1991.

Maslennikov, V.V., Maslennikova, S.P., Large, R.R., Danyushevsky, L.V., 2009. Study of trace element zonation in vent chimneys from the silurian yaman-kasy volcanic-hosted massive sulfide deposit (Southern Urals, Russia) using laser ablation-inductively coupled plasma mass spectrometry (LA-ICPMS). Econ. Geol. 104 (8), 1111–1141. https://doi.org/10.2113/gsecongeo.104.8.1111.

Maslennikov, V.V., Maslennikova, S.P., Large, R.R., Danyushevsky, L.V., Herrington, R. J., Ayupova, N.R., Zaykov, V.V., Lein, A.Y., Tseluyko, A.S., Melekestseva, I.Y., Tessalina, S.G., 2017. Chimneys in Paleozoic massive sulfide mounds of the Urals VMS deposits: Mineral and trace element comparison with modern black, grey, white and clear smokers. Ore Geol. Rev. 85, 64–106. https://doi.org/10.1016/j.oregeorev.2016.09.012.

Maslennikov, V.V., Maslennikova, S.P., Large, R.R., Danyushevsky, L.V., Herrington, R. J., Stanley, C.J., 2013. Tellurium-bearing minerals in zoned sulfide chimneys from Cu-Zn massive sulfide deposits of the Urals, Russia. Mineral. Petrol. 107, 67–99. https://doi.org/10.1007/s00710-012-0230-x.

Mason, T.F.D., Weiss, D.J., Chapman, J.B., Wilkinson, J.J., Tessalina, S.G., Spiro, B., Horstwood, M.S.A., Spratt, J., Coles, B.J., 2005. Zn and Cu isotopic variability in the Alexandrinka volcanic-hosted massive sulphide (VHMS) ore deposit, Urals, Russia. Chem. Geol. 221 (3-4), 170–187.

Mercier-Langevin, P., Hannington, M.D., Dubé, B., Bécu, V., 2011. The gold content of volcanogenic massive sulfide deposits. Miner. Depos. 46, 509–539. https://doi.org/10.1007/s00126-010-0300-0.

Miao, L., Fan, W., Liu, D., Zhang, F., Shi, Y., Guo, F., 2008. Geochronology and geochemistry of the Hegenshan ophiolitic complex: Implications for late-stage tectonic evolution of the Inner Mongolia-Daxinganling Orogenic Belt, China. J. Asian Earth Sci. 32 (5-6), 348–370. https://doi.org/10.1016/j.jseaes.2007.11.005.

Nie, F.J., Jiang, S.H., Zhang, Y., Bai, D.M., Hu, P., Zhao, Y.Y., et al., 2007. Metallogenic Studies And Prospecting Orientation In Central And Eastern Segments Along China-Mongolia Border. Geological Publishing House press, Beijing.

Nozaka, T., Liu, Y., 2002. Petrology of the Hegenshan ophiolite and its implication for the tectonic evolution of northern China. Earth. Planet. Sc. Lett. 202 (1), 89–104. https://doi.org/10.1016/S0012-821X(02)00774-4.

Oudin, E., Constantinou, G., 1984. Black smoker chimney fragments in Cyprus sulfide deposits. Nature 308, 349–353. https://doi.org/10.1038/308349a0.

Piercey, S.J., 2011. The setting, style, and role of magmatism in the formation of volcanogenic massive sulfide deposits. Miner Depos. 46 (5-6), 449–471. https://doi.org/10.1007/s00126-011-0341-z.

Qing, M., Ge, L.S., Tang, M.G., Qu, W.J., Yuan, S.S., Zhao, Y.S., 2011. Molybdnite Re-Os isotope age of Bilihe large-size porphyry gold deposit in Sunid Right Banner of Inner Mongolia and its geological significance. Mineral Depos. 30, 11–20 (in Chinese with English abstract).

Reich, M., Kesler, S.E., Utsunomiya, S., Palenik, C.S., Chryssoulis, S.L., Ewing, R.C., 2005. Solubility of gold inarsenian pyrite. Geochem. Cosmochim. Acta 39, 2781–2796. https://doi.org/10.1016/j.gca.2005.01.011.

Revan, M.K., Genc, Y., Maslennikov, V.V., Maslennikova, S.P., Large, R.R., Danyushevsky, L.V., 2014. Mineralogy and trace-element geochemistry of sulfide minerals in hydrothermal chimneys from the Upper-Cretaceous VMS deposits of the eastern Pontide orogenic belt (NE Turkey). Ore Geol. Rev. 63, 129–149. https://doi.org/10.1016/j.oregeorev.2014.05.006.

Robinson, P.T., Zhou, M.-f., Hu, X.-F., Reynolds, P., Wenji, B., Yang, J., 1999. Geochemical constraints on the origin of the Hegenshan Ophiolite, Inner Mongolia, China. J. Asian Earth Sci. 17 (4), 423–442. https://doi.org/10.1016/S1367-9120(99)00016-4.

Sawkins, F.J., Kowalik, J., 1981. The source of ore metals at buchans: Magmatic versus leaching models. Geol. Assoc. CAN. 22, 255–267.

Sengör, A.M.C., Natalin, B.A., Burtman, V.S., 1993. Evolution of the Altaid tectonic collage and Paleozoic crustal growth in Eurasia. Nature 364, 299–307. https://doi.org/10.1038/364299a0.

Shao, J.A., 1991. Crust evolution in the middle part of the northern margin of Sino-Korean plate. Peking University Press, Beijing.

Shao, J.A., Tang, K.D., He, G.Q., 2014. Early Permian Tectono-Palaeogeographic Reconstruction of Inner Mongolia, China. Acta Petrol. Sin. 30, 1858–1866 (in Chinese with English abstract).

Smith, R.N., Huston, D.L., 1992. Distribution and association of selected trace-elements at the Rosebery deposit, Tasmania. Geol. Bull. Soc. Econ. Geol. 87, 706–719. https://doi.org/10.2113/gsecongeo.87.3.706.

Stolz, J., Large, R.R., 1992. Evaluation of the source-rock control on precious metal grades in volcanic-hosted massive sulfide deposits from western Tasmania. Geol. Bull. Soc. Econ. Geol. 87, 720–738. https://doi.org/10.2113/gsecongeo.87.3.720.

Sun, Y., Zhang, D., Zhang, S., Sun, W., 2009. S, Pb isotopic characteristics and exhalative-sedimentary genesis of Xiaobaliang Cu-Au deposit, Inner Mongolia. Contributions To Geology and Mineral Resources Research. 24(04):282-285+321. (in Chinese with English abstract).

Tang, K., 1990. Tectonic development of Paleozoic foldbelts at the north margin of the Sino-Korean Craton. Tectonics 9 (2), 249–260. https://doi.org/10.1029/TC009i002p00249.

Tanner, D., Henley, R.W., Mavrogenes, J.A., Holden, P., 2016. Sulfur isotope and trace element systematics of zoned pyrite crystals from the El Indio Au–Cu–Ag deposit, Chile. Contrib. Mineral. Petrol. 171, 33. https://doi.org/10.1007/s00410-016-1248-6.

Tornos, F., Peter, J.M., Allen, R., Conde, C., 2015. Controls on the siting and style of volcanogenic massive sulphide deposits. Ore Geol. Rev. 68, 142–163. https://doi.org/10.1016/j.oregeorev.2015.01.003.

Van-Achterbergh, E., Ryan, C.G., Jackson, S.E., Griffin, W.L., 2001. Data reduction software for LA-ICP-MS: appendix. In: Sylvester P. J., editor. Laser Ablation-ICP-Mass Spectrometry in the Earth Sciences: Principles and Applications. Ottawa, Ontario, Canada: Mineralog. Assoc. Canada (MAC) Short Course Series. p. 239-243.

Wan, B.o., Zhang, L., Xiao, W., 2010. Geological and geochemical characteristics and ore genesis of the Keketale VMS Pb-Zn deposit, Southern Altai Metallogenic Belt, NW China. Ore Geol. Rev. 37 (2), 114–126. https://doi.org/10.1016/j.oregeorev.2010.01.002.

Wang, C., 2008. Exhalative Sedimentary Mineralization and Metallogenic Prediction in the Middle-Southern Segment of Da Hinggan Mountains (unpublished Ph.D. thesis). China University of Geosciences, Beijing, Beijing.

Wang, Y., Gao, Y., Santosh, M., Hou, Z., Zhang, H., Xu, S., 2020. Permian dyke swarm with bimodal affinity from the Hegenshan ophiolite-arc-accretionary belt, Central Inner Mongolia: Implications on lithospheric extension in a Carboniferous continental arc. Lithos 356-357, 105369. https://doi.org/10.1016/j.lithos.2020.105369.

Windley, B.F., Alexeiev, D., Xiao, W., Kröner, A., Badarch, G., 2007. Tectonic models for accretion of the Central Asian Orogenic Belt. J. Geol. Soc. London 164 (1), 31–47. https://doi.org/10.1144/0016-76492006-022.

Xiao, W., Windley, B.F., Hao, J., Zhai, M., 2003. Accretion leading to collision and the Permian Solonker suture, Inner Mongolia, China: Termination of the central Asian orogenic belt. Tectonics 22 (6), 1069. https://doi.org/10.1029/2002TC001484.

Xu, B., Charvet, J., Chen, Y., Zhao, P., Shi, G., 2013. Middle Paleozoic convergent orogenic belts in western Inner Mongolia (China): framework, kinematics, geochronology and implications for tectonic evolution of the Central Asian Orogenic Belt. Gondwana Res. 23 (4), 1342–1364. https://doi.org/10.1016/j.gr.2012.05.015.

Xu, B., Zhao, P., Bao, Q., Zhou, Y., Wang, Y., Luo, Z., 2014. Preliminary study on the pre-Mesozoic tectonic unit division of the Xing-Meng Orogenic Belt (XMOB). Acta Petrol. Sin. 30, 1841–1857 (in Chinese with English abstract).

Yang, K.H., Scott, S.D., 2002. Magmatic degassing of volatiles and ore metals into a hydrothermal system on the modern sea floor of the eastern Manus back-arc basin, western Pacific. Geol. Bull. Soc. Econ. Geol. 97, 1079–1100. https://doi.org/10.2113/97.5.1079.

Yu, P., Zheng, Y., 2019. Pb-Zn-Cu accumulation from seafloor sedimentation to metamorphism: Constraints from ore textures coupled with elemental and isotopic geochemistry of the Tiemurt in Chinese Altay Orogen, NW China. Gondwana Res. 72, 65–82. https://doi.org/10.1016/j.gr.2019.02.007.

Yu, P.-P., Zheng, Y., Wang, C.-M., 2020. Trace elemental and sulfur-lead isotopic variations in metamorphosed volcanogenic massive sulfide (VMS) mineralization systems: An example from the Keketale Pb-Zn(-Ag) deposit, NW China. Ore Geol. Rev. 125, 103685. https://doi.org/10.1016/j.oregeorev.2020.103685.

Zeng, Q.-D., Sun, Y.A.N., Duan, X.-X., Liu, J.-M., 2013. U-Pb and Re–Os geochronology of the Haolibao porphyry Mo–Cu deposit, NE China: implications for a Late Permian

tectonic setting. Geol. Mag. 150, 975–985. https://doi.org/10.1017/S0016756813000186.

Zeng, Q., Liu, J., Zhang, Z., Jia, C., Yu, C., Ye, J., et al., 2009. Geology and lead-isotope study of the baiyinnuoer Zn-Pb-Ag deposit, south segment of the Da Hinggan Mountains, Northeastern China. Resour. Geol. 59, 170–180. https://doi.org/10.1111/j.1751-3928.2009.00088.x.

Zhang, H., et al., 1991. The geopyhsical and geochemical survey report of Xiaobaliang Cu-Au deposit, Dong Ujimqin Qi. Inner Mongolia, National Geological Archives of China.

Zhang, X., Li, L.-F., Du, Z.-F., Hao, X.-L., Cao, L., Luan, Z.-D., Wang, B., Xi, S.-C., Lian, C., Yan, J., Sun, W.-D., 2020. Discovery of supercritical carbon dioxide in a hydrothermal system. Sci. Bull. 65 (11), 958–964. https://doi.org/10.1016/j.scib.2020.03.023.

Dehnavi, A.S., McFarlane, C.R.M., Lentz, D.R., Walker, J.A., 2018. Assessment of pyrite composition by LA-ICP-MS techniques from massive sulfide deposits of the Bathurst Mining Camp, Canada: From textural and chemical evolution to its application as a vectoring tool for the exploration of VMS deposits. Ore Geol. Rev. 92, 656–671. https://doi.org/10.1016/j.oregeorev.2017.10.010.

Zheng, Y., Wang, Y., Chen, H., Lin, Z., Hou, W., Li, D., 2016. Micro-textural and fluid inclusion data constraints on metallic remobilization of the Ashele VMS Cu-Zn deposit, Altay, NW China. J. Geochem. Explor. 171, 113–123. https://doi.org/10.1016/j.gexplo.2016.06.015.

Zheng, Y., Zhang, L., Chen, Y., Hollings, P., Chen, H., 2013. Metamorphosed Pb–Zn–(Ag) ores of the Keketale VMS deposit, NW China: Evidence from ore textures, fluid inclusions, geochronology and pyrite compositions. Ore Geol. Rev. 54, 167–180. https://doi.org/10.1016/j.oregeorev.2013.03.009.

Zhou, J.-B., Han, J., Zhao, G.-C., Zhang, X.-Z., Cao, J.-L., Wang, B., Pei, S.-H., 2015. The emplacement time of the Hegenshan ophiolite: Constraints from the unconformably overlying Paleozoic strata. Tectonophysics 662, 398–415. https://doi.org/10.1016/j.tecto.2015.03.008.